TRANSIENT SUPERSONIC METHANE-AIR FLAMES

A Thesis

by

JOHN L. RICHARDS

Submitted to the Office of Graduate Studies of
Texas A&M University
in partial fulfillment of the requirements for the degree of

MASTER OF SCIENCE

May 2012

Major Subject: Aerospace Engineering

TRANSIENT SUPERSONIC METHANE-AIR FLAMES

A Thesis

by

JOHN L. RICHARDS

Submitted to the Office of Graduate Studies of
Texas A&M University
in partial fulfillment of the requirements for the degree of

MASTER OF SCIENCE

Approved by:

Chair of Committee,	Adonios N. Karpetis
Committee Members,	Othon Rediniotis
	Eric Petersen
Head of Department,	Dimitris Lagoudas

May 2012

Major Subject: Aerospace Engineering

ABSTRACT

Transient Supersonic Methane-Air Flames. (May 2012)
John L. Richards, B.S, Colorado School of Mines
Chair of Advisory Committee: Dr. Adonios N. Karpetis

The purpose of this study was to investigate the thermochemical properties of a transient supersonic flame. Creation of the transient flame was controlled by pulsing air in 200 millisecond intervals into a combustor filled with flowing methane. The combustor was designed following well-known principles of jet engine combustors. A flame holder and spark plug combination was used to encourage turbulent mixing and ignition of reactant gases, and to anchor the transient flame. Combustion created a high temperature and pressure environment which propelled a flame through a choked de Laval nozzle. The nozzle accelerated the products of combustion to a Mach number of 1.6, creating an underexpanded transient flame which burned for approximately 25 milliseconds.

Qualitative information of the flame was gathered by two optical systems. An intensified charge-coupled device (ICCD) was constructed from constitutive components to amplify and capture the chemiluminescence generated by the transient flame, as well as the spatial structure of the flame at specific phases. To gather temporal data of a single transient event as it unfolded, a z-type schlieren optical system was constructed for use with a high speed camera. The system resolves the data in 1 millisecond increments, sufficient for capturing the transient phenomenon.

The transient system was modeled computationally in Cantera using the GRI-3.0 reaction mechanism. Experimental conditions were simulated within the zero-dimensional computation by explicit control of the reacting gas mass flow rates within the system. Results from the computational model were used to describe the ignition

process. The major limitation of the zero-dimensional reactor model is homogeneity and lack of spatial mixing. In this work a Lagrangian tracking model was used to describe the flame behavior and properties as it travels within the zero-dimensional reactor towards the nozzle. Following this, the flow expansion through the de Laval nozzle was calculated using one-dimensional isentropic relations. The computed reactor model data was then contrasted to experimental results from the ICCD and high speed schlieren images to fully describe the events in the transient supersonic flame.

DEDICATION

To my family and friends, who never stop supporting me in all of my endeavours.

ACKNOWLEDGMENTS

I would first like to thank my advisor, Dr. Adonios Karpetis, for always being available to discuss a problem and to help me see it through. I can't thank him enough for all of the time and effort he has given to me, through thick and thin. His work ethic is inspiring, and I am honored to have worked under his direction. I would also like to thank Dr. Petersen and Dr. Rediniotis for serving on my committee.

I would also like to thank Alex Bayeh for his assistance with my research, both in and out of the laboratory. He was a constant source of information, and it was a pleasure to work with such a bright individual. I also thank the rest of the research group, Wenjiang Xu and Dean Ellis, for their support.

I would also like to thank the people I hold most dear. I want to thank my fianceé, Renee Francese, for always being there for me whenever I needed it most. I could not have done it without her constant support and motivation. I would also like to thank my parents for their continued guidance and advice. I would not be here today without them. I also thank my sisters for helping me to develop into the person I am today.

Lastly, I would like to thank Tim Cacanindin and the United States Air Force for sponsoring me through the SMART Scholarship program. I owe a great deal of my success to them for all of the opportunities that they have given me.

Thank you to all who continue to inspire me, and motivate me to do better and try harder.

TABLE OF CONTENTS

Page

LIST OF FIGURES

FIGURE Page

FIGURE Page

FIGURE Page

FIGURE Page

FIGURE Page

1. INTRODUCTION

Propulsion science is always expanding into new areas of research. From new areas like electromagnetic propulsion, to the more common combustion based engines, every area is advancing. Supersonic combustion and propulsion are gathering momentum as researchers strive to go faster, higher, and farther, pushing the limits of our current knowledge of aerospace propulsion.

A more common method utilized in aerospace propulsion is the ramjet [1]. By travelling at supersonic speeds, a shock wave forms at the inlet which works to compress the incoming fluid. The increased pressures and temperatures obtained in post shock conditions help to prepare a flow for downstream combustion [2]. However, the main requirement for the ramjet, supersonic speed ($M \geq 1$), can also be the most difficult to obtain. Multiple stages are often required to achieve the supersonic condition, at which point the ram effect continues the acceleration into higher Mach number regimes, as made famous by the Pratt and Whitney J58 engine used on the SR-71 Blackbird [3].

There is a possible method for mitigating the use of multiple staged engines using one robust engine solution with transient pulsed pressure waves, as seen in Figure 1.1. The shock wave needed for combustion in a ramjet engine may be synthesized through pulsed pressure waves. The interaction of weak pressure waves applied at a nozzle inlet could potentially interact to form a strong shock within the duct. This strong shock can be formed at subsonic speeds, and would prepare a flow for combustion. This would greatly reduce the speeds needed to operate a ramjet engine ($M < 1$). Other major advantages to such an engine include safety, and the lack of moving parts which will drastically lower overall operating costs. The motivation behind the present work is to examine the possibility of using a pulsed supersonic flame as a generator of these weak pressure waves.

This thesis follows the style of *Journal of Propulsion and Power*.

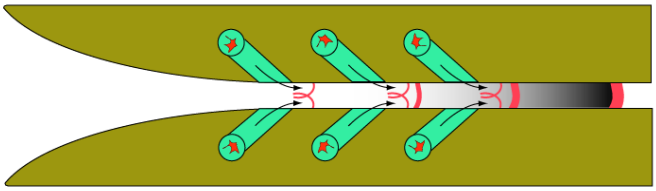

Fig. 1.1. Proposed solution for construction and operation of a low speed ramjet engine. Pulsed pressure waves interact and coalesce to form a normal shock within the duct, preparing a flow for combustion.

An important research area in propulsion science today involves transient processes. Steady state combustion has long been studied and used in engines, but transient processes are now being examined to determine their abilities in propulsion systems. One of the main ideas for transient propulsion involve pulsed detonations, and are referred to as pulsed detonation engines (PDE) [4, 5]. Although the theory behind their use is sound, the implementation can be quite dangerous due to the high pressures involved with their operation. Pulsed jets have also been studied, mainly for use in supersonic combustion ramjets (scramjets) [6–8]. These pulsed supersonic jets are typically used for flow control, or for fuel injection into scramjet engines. However, the principles used in the pulsed jets are generally related to detonation tubes.

A safer approach to creating the transient pressure waves may be found using pulsed supersonic flames. The present work will examine the creation of a pulsed supersonic flame through actuation of the incoming oxidizer. The pulsed actuation is achieved using an electromagnetic solenoid which controls the flow of air into the combustor. With correct timing the system will ignite, providing a high pressure, supersonic flame at the combustor exit. Other methods for pulsed air systems have been explored, but the electromagnetic solenoid was chosen for its cost and ease of implementation [9, 10].

The combustor used in the experiment is constructed using jet engine principles, and uses a flame holder to promote turbulence and stabilize a flame. The effects of flame holders has been well researched since the 1950s for use in jet engine configurations [11–13]. Additionally, a de Laval nozzle is used to accelerate the flame to supersonic speeds. Converging-diverging nozzles have also been well documented for use in rockets and jet engines [2, 14, 15].

Information on flames is often gathered optically. Two optical methods used in this experiment are an Intensified CCD (ICCD) and a schlieren system. Both of these methods have been used extensively for combustion research. The ICCD is often used in conjunction with laser based solutions for induced fluorescence, providing measurements of molecular constituents in the flame [16, 17]. However, the present work is more concerned with gathering photons created through chemiluminescence, the natural emission of light from a flame. Chemiluminescence has also been detected using ICCD systems, typically with different sets of filters applied to better resolve the concentrations of certain species in a flame [18, 19]. The present work focuses primarily on the qualitative aspects of the transient flame, although optical filters can be applied to the ICCD in the future. The schlieren setup is also used extensively in laboratories [20, 21]. A schlieren setup is appealing to combustion processes due to the ability of the system to detect density gradients produced by both high speed flows, and combusting gases [22, 23].

The flow pattern of a supersonic jet has been observed since the early 1900s, but is still important today. The structure of the supersonic jet can be an indication of the performance of a nozzle, but can also be observed to understand combustible areas within the flow [24]. The shockwave interactions for under and overexpanded jets are well defined in literature [2, 14].

This thesis is divided into sections. Section 2 details the experimental setup used to produce the transient supersonic flame, and the numerical model that mimics the experimental system. Included in this section is the description of gas regulation for

the experimental system, as well as the design of the combustor. Additionally, the computational model of the experimental system is described. Section 3 discusses the design and creation of the two optical systems used to image the transient supersonic flame. Section 4 concludes this thesis by presenting and discussing the results obtained both visually and computationally.

2. TRANSIENT SUPERSONIC FLAME APPARATUS AND SIMULATION

In what follows, the design, construction, and simulation of the transient supersonic flame apparatus is discussed. The combustion chamber was based on previous work in creating miniaturized combustors for afterburner flames [25]. The present system is a transient extension of the existing steady state device. The transient nature was discovered when unburnt flow through the nozzle was blocked using a thin walled obstruction [26]. The stagnation would allow a flammable mixture to form, creating a transient flame which would burst through the obstruction. The new device is operated transiently through the use of an electromagnetic solenoid valve. The valve actuation is designed to mimic the blocking effect of the obstruction. Chemilluminescence is desired because it is natural light emitted from the flame, allowing for observation without laser assistance. In terms of light emitted, supersonic flames are not very robust. Transient flames compound this problem, due to the small timescales in the experiment. The apparatus is simulated using Cantera, an open source software package, providing detailed chemistry and thermodynamic information. The program will be used to understand the behavior of thermochemistry within the combustion chamber throughout the transient event.

2.1 Supersonic Flame Apparatus

Due to the high pressures and temperatures that occur within the combustion chamber, materials that were able to withstand flame conditions were required. For this reason, brass and stainless steel components were used. These components were selected for their ease of use, availabilty, and machineability. The thermal coefficients of expansion between the two materials are similar, mitigating any problems inherent in heating dissimilar metals. In addition, high temperature thread locking material is applied to prevent any gas leaks during the combustion process.

The combustion chamber features three distinct sections. The outer chamber, the flame tube, and the nozzle, as shown in Figure 2.1. Methane is injected directly into the central flame tube. The tube contains a bluff body stabilizer (flame holder) combined with a spark plug in the recirculation region to initiate combustion [27]. The 90° vee-shaped bluff body occupies approximately half the area in the flame tube and is placed directly at the center of the flow. Assuming a maximum velocity of 10 m/s through the flame tube, and for an incompressible flow, the bluff body obstruction woud create a pressure drop of less than 100 Pa. Therefore, the pressure drop across the blockage is neglected due to the low velocities within the combustion chamber. The recirculation region can be estimated as a wedge-shaped body, with a characterized length as a parameter of bluff body height and flow velocity [13]. This region will be discussed in Section 4.2.

The initial construction of the combustor was based on designs for vitiated-air jet engines. Air is injected into the outer chamber via a solenoid valve, and is allowed to

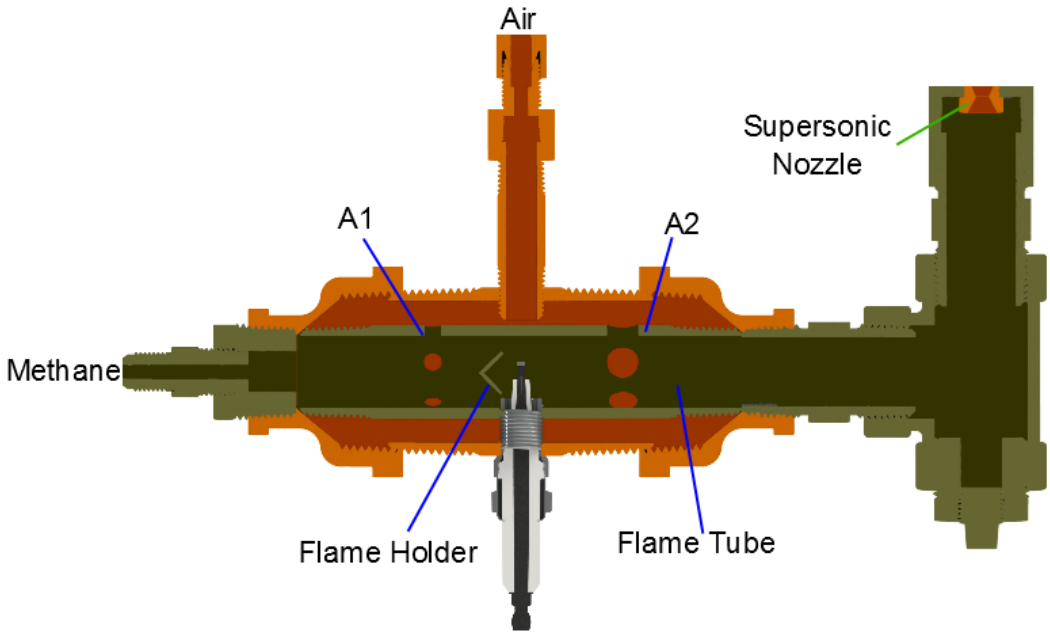

Fig. 2.1. Section view of computer generated combustor assembly.

mix with the methane through two entry areas (A1 and A2). The electromagnetic solenoid has an opening/closing time in the order of 25 ms. This relatively fast actuation will provide the appropriate air transient for combustion. The primary and secondary regions are a circular pattern of holes, with a secondary/primary area ratio of 3.3, as seen in Figure 2.1. Although the air inlets were initially designed to mimic air inlets on a jet engine, the actual operation is much different, and will be discussed in later sections.

Mass flow rates are metered by choked orifice plates at the methane and air supply tanks. The combination of orifices would result in a steady state equivalence ratio of $\phi = 1.4$, less than the upper flammability limit of 1.7 for methane [28]. However, the transient nature of the system yields an equivalence ratio that is continually changing throughout the actuation process. As the solenoid begins to open ($t \simeq 0$ ms), the area restriction at the solenoid produces a choked flow. As time progresses ($t > 0$ ms), pressure will build within the chamber, allowing for mixing of reactant gases. At this point, the air recirculates within the volume created by the flame holder, mixing with the methane and allowing combustion to occur.

After ignition, the products of combustion are then accelerated downstream through a de Laval nozzle. The de Laval nozzle expands the flow past $M = 1$, producing supersonic flow at the nozzle exit. The throat diameter is the smallest area in the combustion chamber to ensure choking after the air and fuel have been mixed. After undergoing a slight area expansion, the reacting gases are exhausted to the atmosphere. The ratio of exit area to throat area (ϵ expansion ratio in rocket science) is 1.25. Using the following 1-D isentropic expansion equation, the Mach number at the exit can be found.

$$(\frac{A_{exit}}{A_{throat}})^2 = \frac{1}{M^2}[\frac{2}{\gamma+1}(1+\frac{\gamma-1}{2}M^2)]^{\frac{\gamma+1}{\gamma-1}} \tag{2.1}$$

where M is Mach number, A_{exit} and A_{throat} are the exit areas and nozzle throat areas, and γ is the ratio of specific heats for the fluid [2]. The resulting Mach number at the nozzle exit is $M = 1.6$.

The nozzle is constructed from superfine isomolded graphite. The properties of graphite make it ideal for use in rocket nozzles [14]. Graphite experiences minimal shape change when heated, making it optimall for use in the transient combustion environment where the nozzle is constantly being quickly heated/cooled. Additionally, this property ensures that heat based fracturing will not occur, mitigating the constant replacement of nozzles. Temperatures required for the ablation and sublimation of graphite are in excess of 3800 K [29]. This is much higher than the temperatures reached within the combustion chamber, as will be shown in later sections. The temperature never exceeds 2700 K, and that is observed only during short durations throughout the transient burn. The small timescales of the transient flame mitigate the effects of erosive burning on the nozzle area ratio (Equation 2.1). Therefore, erosive burning of the nozzle surface is neglected due to the transient nature of the experiment.

The spark plug used to ignite the system is driven by an ignition coil which is charged by a 13.8V 15 Amp power supply. The key element to creating a high voltage spark is the rapid change of current through the ignition coil. This is achieved using a 2N3055 NPN transistor. Unlike a mechanical relay, the transistor allows for fast changes in current flow, creating voltages in the ignition coil upwards of 15 kV, ensuring a very energetic spark.

The various timescales of the experiment require accurate time coordination. The system timing can be controlled using two different methods, a) through the use of an in-house built timing circuit, or b) by using a Berkeley Nucleonics 565 pulse generator. The first method requires a set of circuits designed around the LM555 timer integrated circuit (IC) operating in cascading monostable mode. The second method uses a pulse generator which has an array of individually controlled channels

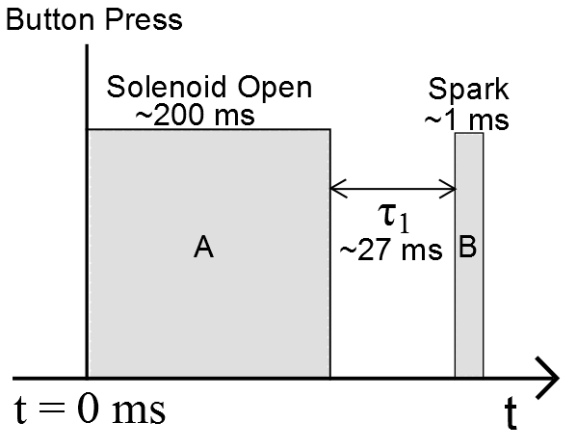

Fig. 2.2. Relative timescales used in the experiment. (A) represents the open solenoid time (∼200 ms), and (B) is the ignition spark (∼1 ms). The experiment is initiated by a button press. The delay (τ_1) determines the ignition point, and is required for allowing the reactants to mix before combustion.

through which 5 V Transistor-Transistor-Logic (TTL) signals can be generated. The goal is to control the timescales used in the experiment. The timing revolves around a master signal, in this case the solenoid valve. The length of the master signal indicates the amount of time the solenoid is open for, as seen in Figure 2.2. A second pulse is used to trigger the ignition spark. The delay time between the solenoid closing and the spark must also be tuned to ensure combustion occurs, as will be discussed in Section 4.1. A third trigger is needed for the image intensifier and is described in Section 3.1.

The methane and air flows are provided by regulated tanks far upstream of the combustor. Orifice plates are used to control the mass flow rates of the methane and air just downstream of the pressure regulators. The orifices ensure a flammable mixture during the ignition process. Total pressure at the regulator can be varied between 60–120 psig for the experiment. These bounds are predetermined by experimental conditions; the solenoid valve cannot withstand upstream tank pressures

above 120 psig, and the combustor nozzle will not choke at a tank pressure below 60 psig, according to the result described in Equation 2.3.

By monitoring the pressure upstream and downstream of the orifices, the appropriate flow regime can be determined as either sonic or subsonic. The flow rates differ greatly depending on the flow regime. The sonic mass flow rates through the orifice are calculated using the 1-D isentropic compressible flow equation:

$$\dot{m} = \frac{AP_t}{\sqrt{T_t}}\sqrt{\frac{\gamma}{R}}\left(\frac{\gamma+1}{2}\right)^{-\frac{\gamma+1}{2(\gamma-1)}} \tag{2.2}$$

where A is the area of the orifice, p_t is the total pressure upstream of the orifice, T_t is the total pressure, γ is the ratio of specific heats, and R is the specific gas constant [14]. A flow is choked when the Mach number of a system reaches unity. In the absence of heat transer and friction, this point will almost always occur at the minimum area of the system. The flow will become choked when the pressure located at the minimum area (throat pressure) reaches a critical value dictated by isentropic relations. The critical pressure required for choked flow is described by the following 1-D isentropic relation:

$$\frac{P^*}{P_t} = (\frac{2}{\gamma+1})^{(\frac{\gamma}{\gamma-1})} \tag{2.3}$$

which for air at $\gamma = 1.4$, is 0.528 [30]. If the throat pressure reaches the critical pressure, P^*, choked flow at the metering orifice can be assumed [2]. In the case of the methane, air, and solenoid orifices, the throat pressure while subsonic can be assumed to be the same as the downstream pressure, simplifying the equation.

The overall reacting gas delivery system is depicted in Figure 2.3. It is important to note that when pressurized, the solenoid valve will act as an orifice. Therefore, the pressure distributions throughout the system become increasingly complex with actuation of the solenoid valve. The presence of the solenoid valve in the air supply line does not ensure that the upstream orifice is choked. In the air supply line, the

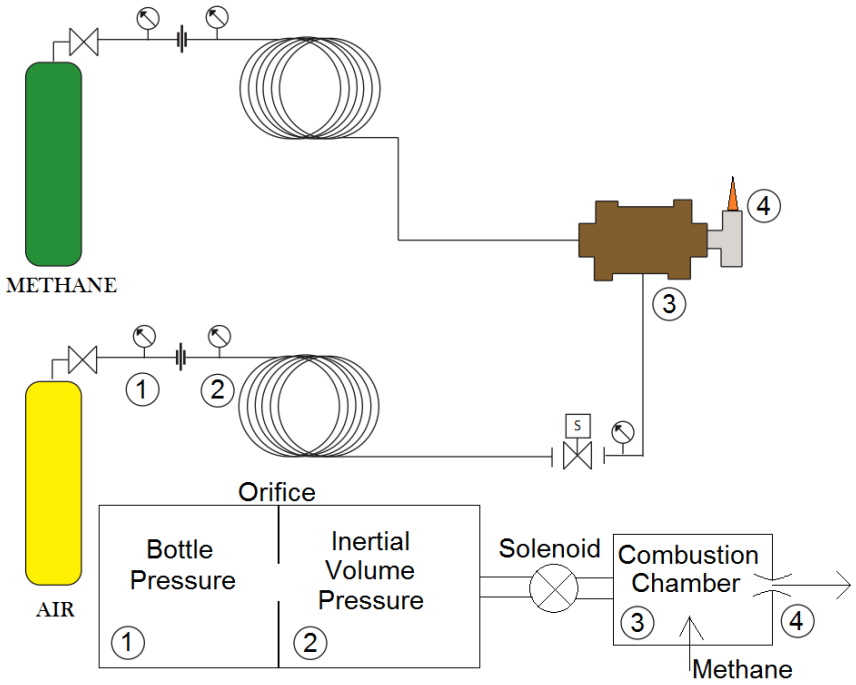

Fig. 2.3. Diagram of reacting gas delivery system and depiction of general volumes encountered in the air supply line.

flow can only choke at one area in steady state configurations, either the orifice or the solenoid. The choke point will vary in time as the system pressures and the area of the solenoid in the air line change. As the pressure builds in the air supply line the orifice will cease choking. When flow through an orifice is subsonic, a mass flow rate can be described using an inviscid approach.

$$P_1 - P_2 = \frac{1}{2}\rho V^2 \tag{2.4}$$

where P_1 and P_2 correspond to upstream and downstream pressure, V is the velocity, and ρ is the density. Because the flow is subsonic, it can be assumed the the flow is

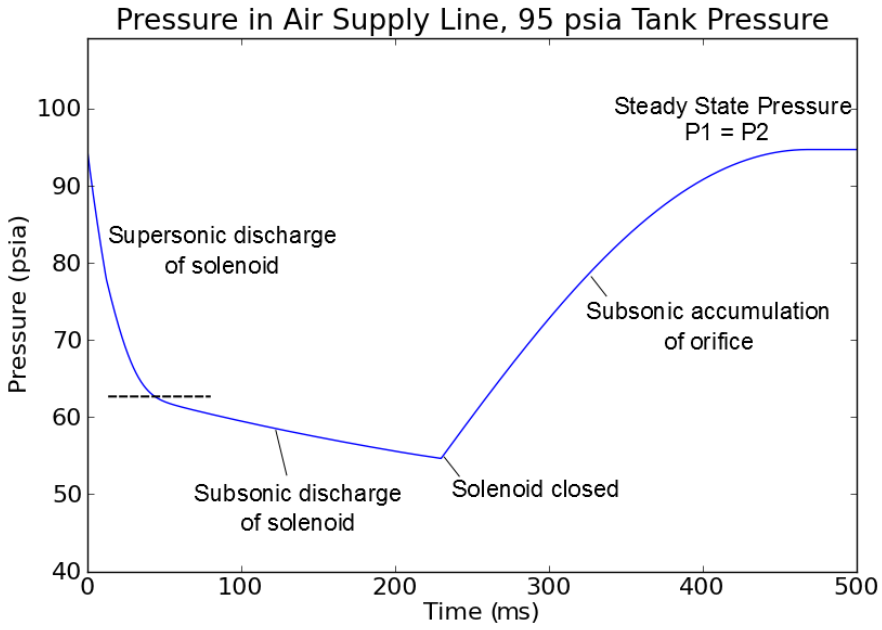

Fig. 2.4. Graph representing an example of pressure within the inertial volume during solenoid actuation. Note the separate regions of subsonic/supersonic flow.

incompressible. Therefore, density in this case can be considered constant. Solving for velocity, the mass flow rate can be found using the definition of mass flow rate:

$$\dot{m} = \rho V A = \sqrt{2\rho(P_1 - P_2)}A \tag{2.5}$$

where A is the area of the orifice.

The presence of a solenoid valve at the combustion chamber, which acts to quickly start and stop the supply of air, will cause the volume between the supply tank and solenoid valve to become pressurized. This pressurized system has an inertia that must be taken into account when simulating the combustion process, as it will greatly affect the combustion system pressure, as shown Figure 2.4.

Although there will be a temperature loss due to the expansion of gases through their respective orifices, the surface area of the supply lines will ensure that enough

heat transfer will occur to keep the gas at ambient temperatures. The exception to this is the mass flow rate through the nozzle, as the temperature of the combustion chamber can not be assumed ambient at all times. The thermodynamic properties of the combustor are calculated by the software package described in Section 2.2 to calculate the nozzle mass flow rate.

Figure 2.4 shows the pressure distribution within the inertial volume for one of the operating conditions of the experiment (corresponding to a tank pressure of 95 psia). The solenoid opens at time t =0 s, causing the supersonic discharge of air due to the relatively large choked area of the solenoid. Because the combustion chamber has a nozzle with a small throat diameter, there will be an accumulation of pressure in the combustion chamber. As the pressure in the chamber rises the solenoid orifice will stop choking, causing subsonic discharge through the solenoid orifice. The lowered pressure in the inertial volume will cause the air orifice upstream of the solenoid to begin flowing, attempting to replenish the volume created in the air supply line. Due to the large area of the solenoid orifice, steady state conditions would result in choked flow through the air orifice, and subsonic flow through the solenoid. When the solenoid begins to close at approximately t = 200 ms, the inertial air supply volume will fill as it did before $t = 0$ ms, eventually reaching a steady state pressure corresponding to the back pressure of the system, as shown in Figure 2.4.

2.2 Combustor Simulation

The combustor is simulated as a zero-dimensional well-stirred reactor (WSR) using Cantera [31]. Cantera is a suite of object-oriented software tools used for chemically reacting flow problems involving chemical kinetics, thermodynamics, and transport processes [32]. The present work uses the Gas Research Institute Mechanism 3.0 (GRI-Mech 3.0), which is an optimized detailed kinetic mechanism based on experimental measurements designed to model methane-air combustion [33]. It utilizes 325 mostly reversible reactions and 53 gas species. This work is performed

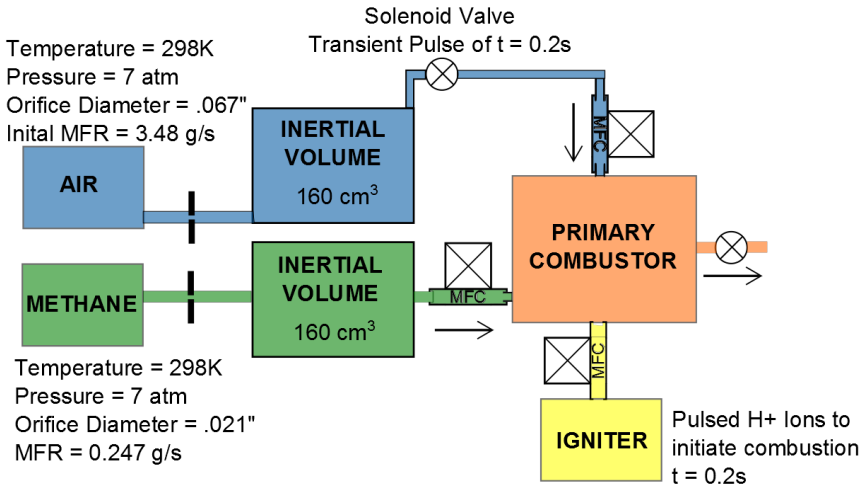

Fig. 2.5. Basic diagram of combustor simulation within Cantera.

using Python 2.6, an object oriented programming language with various scientific and mathematic library packages available [34]. Comparisons of simulated reactor based combustion experiments with Cantera have been performed, but the literature on the topic is scarce [35]. However, the code has been validated in certain geometries against experimental data [35]. The present study will use the results only in a qualitative sense, in order to explain the observations in the experiment. Therefore, questions of computational accuracy do not arise.

The zero dimensional model assumes that gases are instantaneously mixed, regardless of the vessel size or the pressure differences and velocities across the reactor. This introduces several discrepancies in the comparison of the experiment to the simulation. Assumptions must be made to ensure congruency between the physical device and the simulation. The volume of the combustor is estimated to be 120 cm^3. The overall system is modeled in Cantera as shown in Figure 2.5. The ignition event is mimicked by injecting hydrogen atoms into the flow. The extreme reactivity of these atoms initiates combustion. The hydrogen atoms have a profound effect on a transient system. The mass flow rate profile for hydrogen is in the shape of a Gaussian pulse, as a function of time. Due to the transient nature of the system, the

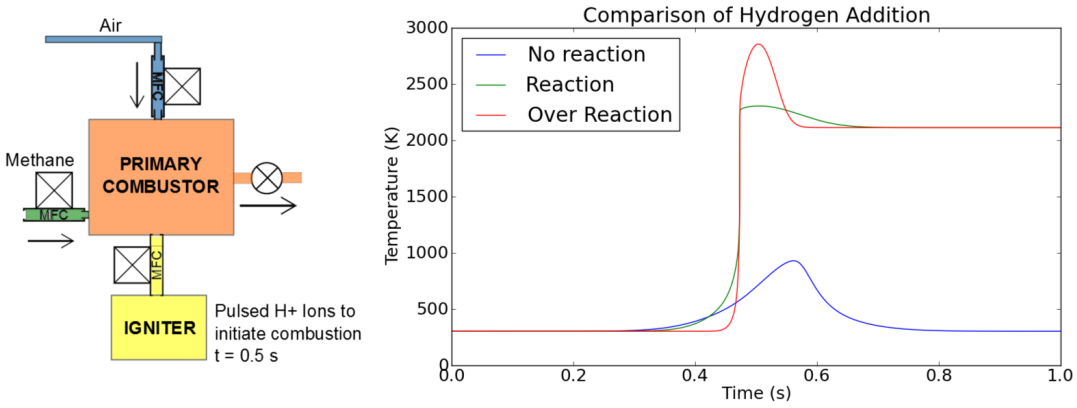

Fig. 2.6. Effect of hydrogen atom injection on a simulated steady state system. Case A) Not enough hydrogen atoms added, no reaction occurs. Case C) Too many hydrogen atoms are added, resulting in an inaccurate temperature spike with reaction. Case B) The correct amount of hydrogen atoms are added, resulting in a reaction with a small transient temperature spike. Time in this case is not related to the times used in the rest of the figures.

characteristics of the pulse had to be carefully selected because of how it affects the simulation, as seen in Figure 2.6. Atoms are literally added to the flow, and begin affecting the chemistry and thermodynamic properties of the gas as soon as they are injected.

As shown in Figure 2.1, there are two injection regions for air into the system (A1, A2), which necessitate the use of two different combustor volumes for the simulation. However, the complexities that the two area ratios of the combustor pose led to the adaptation of the single volume model shown in Figure 2.5. Although Eularian simulations have been performed using bluff body stabilized flames, the transient nature of the calculation will assume a Lagrangian moving flame volume, and will be discussed in Section 4.2 [36]. The final combustion products are exhausted to an infinite reservoir, mimicking atmospheric conditions. The supply tanks are located 40 feet away from the experiment, necessitating the inclusion of large inert volumes for which the air and methane can occupy before flowing into the combustor. The

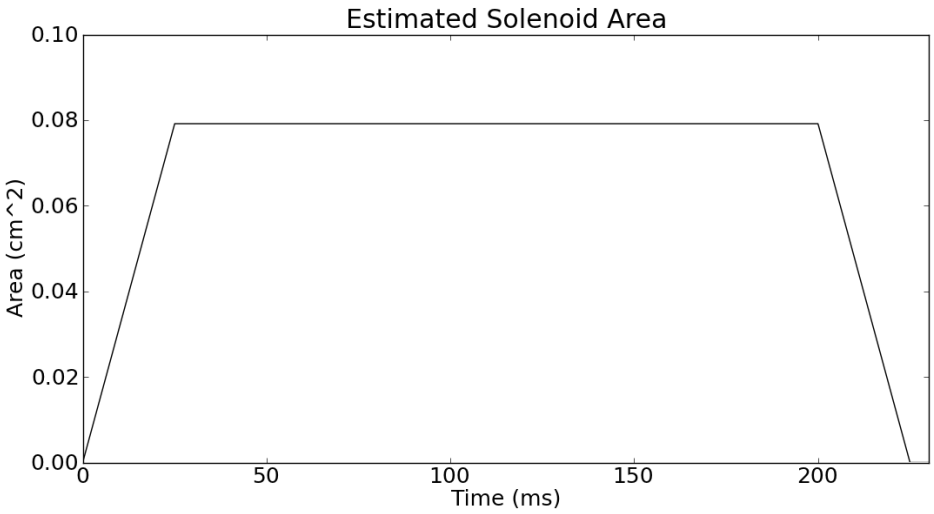

Fig. 2.7. Representation of the solenoid orifice area as a function of time. The 25 ms opening and closing timescale is depicted linearly for the opening and closing actuation.

role of the inertial volume is important, as pressure effects heavily influence the experiment, and therefore must be accounted for within the simulation. Although there is an inertial volume in the methane supply line, the effects of this volume are neglected. The relative orifice area of the methane is small enough to ensure that it will always be choked, and will therefore be providing a constant mass flow rate. For this reason, the inertial volume in the methane supply line is neglected.

Because the solenoid is a mechanical system, there is a physical timescale associated with opening and closing the device. This timescale is approximated to be 25 ms. During this period, the solenoid orifice area is changing, greatly affecting the mass flow rate ($\dot{m}_{sol}$) through the device. In an ideal case, the solenoid would open instantaneously, allowing air to move through it at a rate proportional to the upstream pressure, as shown in Figure 2.4. In reality, the 25 ms opening time will create a "pulse" discussed in later sections. This pulse is the result of the high pressure air in the inertial air supply volume being discharged into the combustion chamber. The solenoid connecting the high pressure inertial volume to the combus-

tor will be choked until the pressure in the inertial supply volume drops below the critical value for choking, described by Equation 2.3. When the solenoid is no longer choked, the mass flow rate ($\dot{m}_{sol}$) will be equivalent to the choked value of the air orifice ($\dot{m}_{Air}$). The area change of the solenoid is modeled in time, as shown in Figure 2.7. The opening and closing times are described as linear slopes for simplification of the problem. The area described is used in Equations 2.2 and 2.5 to calculate the mass flow rate of the solenoid ($\dot{m}_{sol}$).

3. EXPERIMENTAL TECHNIQUES

Imaging the transient flame phenomenon poses many difficulties due to the small timescales present in the experiment, and the generally low light conditions in the flame. Unlike laser-induced methods which generate photons, the present work relied on chemiluminescence, i.e. the emission of light as a result of chemical reactions. These complications were dealt with via two different methods which were applied to the transient flame.

3.1 The Image Intensifier

The main benefit of the image intensifier the ability to amplify the number of photons emanating from an experiment. This experiment used a 3rd generation (Gen III) ITT Night Vision image intensifier (FS9910C). An image intensifier has three primary components within its housing: the photocathode, the photoanode, and the microchannel plate (MCP) [37]. In this particular intensifier, gallium arsenide is used as the photoelectric material in the photocathode, and a P43 phosphor was used for the photoanode [38].

The quantum efficiency (QE) of an image intensifier is based on the photoelectric materials utilized, and is defined as:

$$QE = \frac{\#Photoelectrons}{\#Photons} \tag{3.1}$$

Gen III image intensifiers are known for their high QE, which can be in excess of 50% depending on the observed wavelength and the properties of the photoelectric material used [37]. The spectral response curve of the gallium arsenide photocathode is nearly flat for wavelengths of 450 nm–850 nm, ideal for imaging any flame in the visible spectrum.

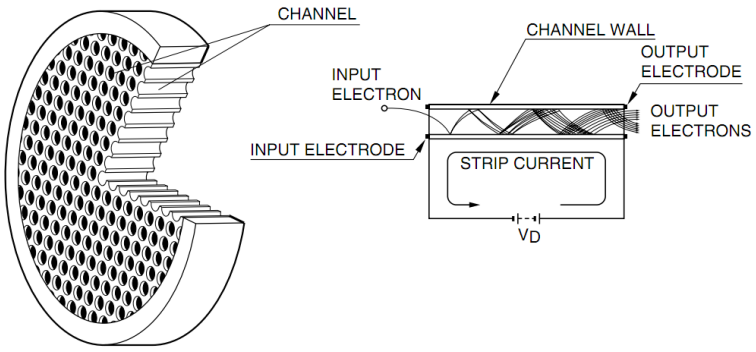

Fig. 3.1. Diagram of a Microchannel Plate (MCP), reproduced with permission from Hamamatsu Photonics [37].

The MCP is constructed using a glass wafer, which contains thousands of small glass tubes or slots, as shown in Figures 3.1 and 3.2 [37]. As the electrons enter the electrically charged MCP and ricochet through the channels, they are multiplied by making contact with the sidewalls of the tube [37]. The number of electrons generated is proportional to the voltage differential across the MCP. The outgoing electrons then strike the photoanode which emits photons to be captured either by eye or photodetector. The gain of the system is adjustable by altering the voltage differentials of either the photocathode, or the MCP.

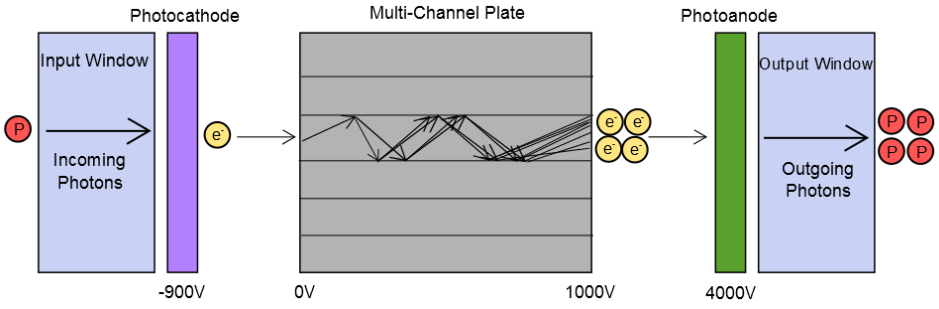

Fig. 3.2. Diagram of the operation of an image intensifier.

The photocathode is the most important component in regards to the transient supersonic flame. Timing is brought into the system by the methods mentioned in Section 2.1. The photocathode must be quickly pulsed to achieve optimal results. If it is not pulsed quickly enough, a "smearing" effect will appear in the photos taken. However, pulsing too fast could limit the amount of entering light, causing dim or noisy photos. There is a balance that must be found experimentally. The optimal gating value was found to be between 1–3 ms. Other experiments typically utilize laser induced methods for increasing light levels, providing intensifier gates as low as 2 ns [16]. Although the image intensifier was capable of gates as low as 20 ns, the low light from the experiment required the larger gate to capture the event with minimal noise.

High voltages are provided by an in-house built power supply, which utilizes a high voltage pulser for the photocathode, and a steady state high voltage power supply for the differential voltages across the MCP and photoanode, as shown in Figure 3.3. A 24V DC power supply provides energy for both the steady state high voltage power supply and the high voltage pulser. The high voltage pulser can be tuned between -500 V and -900 V, providing an extra gain control on the photocathode if desired. It is triggered by a TTL signal provided by either of the signal generators listed in Section 2.1, allowing precisely timed gating of the image intensifier. The steady state power supply provides an 8 kV potential, which was split using a voltage divider network, providing separate voltages for the MCP and photoanode. Low current needed to be ensured to keep from burning out the power supply, so resistance values in the $M\Omega$ range were chosen for use in the divider network. The fractions in Figure 3.3 show relative values that were used.

3.2 Charge-Coupled Device

CCDs operate using electronic shift registers to move an electrical charge out of the CCD pixels and into an A/D converter for digitizing the signal obtained [39].

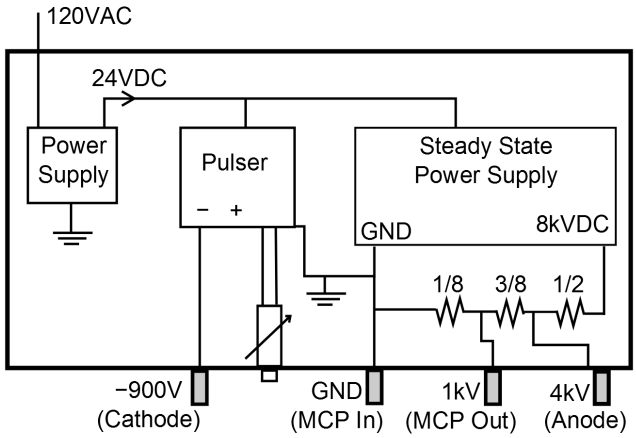

Fig. 3.3. Schematic of image intensifier power supply unit. The pulser has a variable resistor that provides voltage tuning of the negatively charged pulse. The voltage divider resistor network utilizes $M\Omega$ valued resistors, depicted as fractions to convey relative resistor values. The provided voltages apply to the intensifier depicted in Figure 3.2.

CCDs are often used for scientific purposes in large part due to their typically high quality photo-imaging abilities, pixel binning options, and cooling capabilities. Most CCDs present a high quantum efficiency of 60% or more (90% for state of the art CCD systems), with uniform and reproducible images, making them ideal for the laboratory environment.

A Santa Barbara Instruments Group (SBIG) Pixcel 255 (ST-5) astronomical detector was used to obtain intensified images of the emerging flame fronts. The images were gathered through CCDOps, a proprietary imaging software created by SBIG [40]. The ST-5 has a resolution of 320x240 pixels, with a pixel size of 10x10 μm [41]. The ST-5 was chosen because of its thermoelectric cooling abilities, mounting style, software support, and picture quality, all of which is related to the original purpose of astronomical imaging. Additionally, astronomical CCDs typically offer high signal to noise ratios (SNR = S/N), comparable to scientific CCDs.

The noise $\dot{N}$ of any shot-limited signal can be related to the actual signal, represented as photon counts $\dot{P}$ by the formula $N \sim P^{1/2}$. The SNR for such a simple system then follows as $SNR \sim P^{1/2}$, stating that an increase in signal levels will create a small increase in SNR [38]. However, physical systems contain more sources of noise which can be accounted for in the following equation:

$$SNR = \frac{\dot{P}Q\tau}{[(\dot{P} + \dot{B})Q\tau + \dot{D}\tau + N_{A/D}^2]^{1/2}} \tag{3.2}$$

where $\dot{P}$ is the rate of arriving photons (s^{-1}), $\dot{B}$ is the arrival rate of background photons (s^{-1}), $\dot{D}$ is the electron generation rate from thermal effects on the CCD (dark current, in s^{-1}), $N_{A/D}$ is the read-out noise that is generated during the Analog-to-Digital conversion process (unitless), Q is the quantum efficiency of the detector (unitless), and τ is the exposure time of the image [38]. An image intensifier increases the output gain of incoming photons, which can be represented in the SNR as G:

$$SNR = \frac{G\dot{P}Q\tau}{[(\dot{P} + \dot{B})GQ\tau + \dot{D}\tau + N_{A/D}^2]^{1/2}} \tag{3.3}$$

Minimizing the noise sources is essential to improving the quality of the images obtained. At least two of the noise sources can be attenuated. The background photons are eliminated in three ways, by operating within a light-tight area (reducing $\dot{B}$), by using short exposure times on the CCD (reducing τ), and by gating the image intensifier (also reducing τ). Dark current noise can be minimized using thermoelectric cooling, which is pre-installed on the ST-5 (reducing $\dot{D}$). The camera can cool the CCD to a steady state value of -17°C, drastically increasing the SNR of the camera. Pixel-binning is not supported by the ST-5, therefore the read-out noise cannot be eliminated.

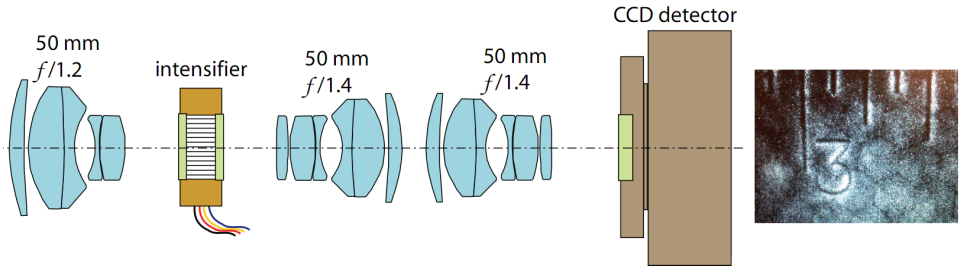

Fig. 3.4. Two dimensional representation of the coupling of the image intensifier to the CCD. Note the honeycomb shapes in the output image. These cells are unique to Gen III intensifiers. A protective film is placed on the photocathode to prevent electrons from flowing back into the photocathode. The honeycomb shapes are from the metal grid that supports the protective film.

3.3 Optical Relay

Typically, an image intensifier is fitted to an imaging system by a fiber optic plate. In this work, an optical relay consisting of multiple lenses was used instead. Despite the higher efficiencies obtained through fiber optic coupling, the optical relay was chosen due to its cost savings, versatility in the lab environment, and the inherent difficulty of applying a fiber optic plate to the intensifier output window. However, several problems arise when attempting to couple the intensifier to a CCD.

Lenses typically mount to a CCD using specifically designed connectors that vary between manufacturers. For this reason, Nikon lenses were exclusively used to ensure congruency when mounting components. Every lens has a specified register, which is the distance from the mounting ring to the focal point of the lens. This value is extremely precise and must be respected, as any errors will greatly influence the focusing of the optical system. Nikon lenses have a register of 46.5 mm with an F style optical mount [42].

The image intensifier provides an input/output window for observation, necessitating careful coupling of the Nikon lenses. A schematic of the system is shown in Figures 3.4 and 3.5. The f number of a lens is defined as f/D , where f is the

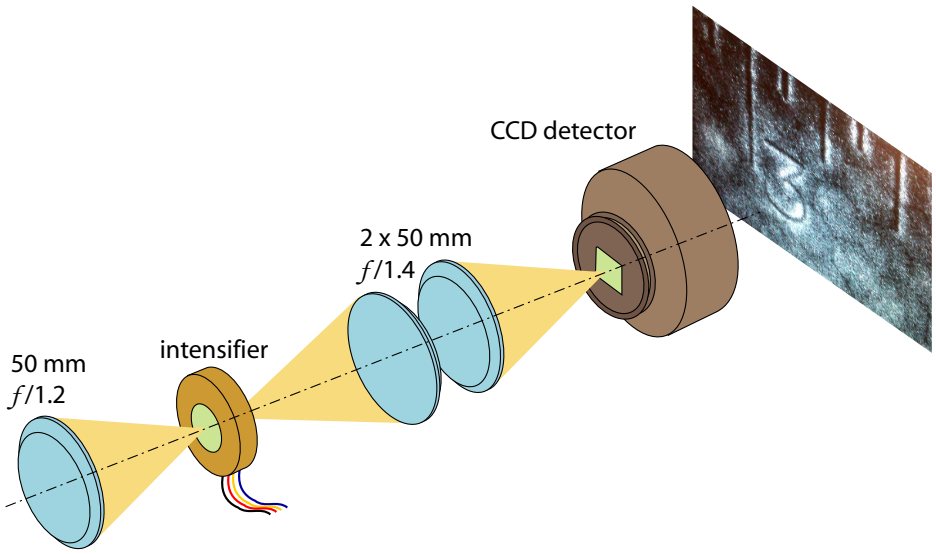

Fig. 3.5. Three dimensional representation of the optical relay system.

focal length of the lens, and D is its diameter. More light can be captured using a lower f number, because of the larger solid angle of collection. The amount of light transmitted through a lens will decrease with the square of the f number [43]. A Nikon prime f/1.2 is used as a collecting lens on the front of the system, as it will capture the most light for the intensifier. The f/1.2 must be placed exactly 46.5 mm away from the input window of the intensifier to ensure proper focus of the system.

The image from the output window of the intensifier is relayed to the CCD through two f/1.4 lenses placed front-to-front, as seen in Figures 3.4 and 3.5. The front-to-front method helps to cancel the geometric abberations introduced when working with spherical lenses. When planar light enters a spherical lens, the wavefronts at the exit become spherical [44]. Naturally, running the spherical wavefronts backwards through the same lens reverses the process, producing a planar image once more. The planar image is focused onto the focal plane array (FPA), completing the relay. The f/1.4 lenses are focused at infinity, allowing for 1:1 image conjugation from the intensifier to the CCD.

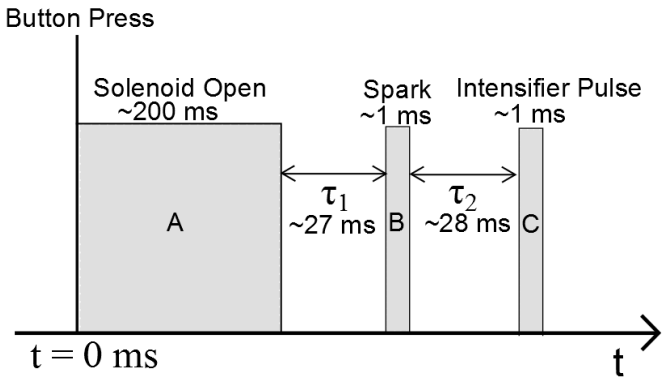

Fig. 3.6. Relative timescales used in the experiment. (A) represents the open solenoid time (∼200 ms), (B) is the ignition spark (∼1 ms), and (C) is the activation duration of the image intensifier (∼1 ms). The experiment is initiated by a button press. The delay (τ_1) determines the ignition point, and is required for allowing the reactants to mix before combustion. The second delay (τ_2) determines which phase of the flame is captured. $\tau_2 = 28$ ms corresponds to the flame emergence from the nozzle.

3.4 Intensifier Timescale

The assembly of the intensifier system adds complexity to the timing system described in Section 2.1. The intensifier will require a gated signal in order to trigger the device, as discussed in Section 3.1. Figure 2.2 must now be updated to reflect the addition of the ICCD. The optimal trigger value for the photocathode pulser was experimentally determined to be between 1–3 ms. In order to capture the chemiluminescence from the emerging flame, a delay time is needed for the intensifier. The flame will take a certain amount of time to travel through the combustor and finally arrive at the nozzle, and will be discussed in Section 4.2. When it arrives at the nozzle, the ICCD can then capture the light. The flame travel time, or intensifier delay, was experimentally determined to be ≈ 28 ms. This new delay time can now be added to the timing system, expressed in Figure 3.6.

3.5 Intensified Image Data

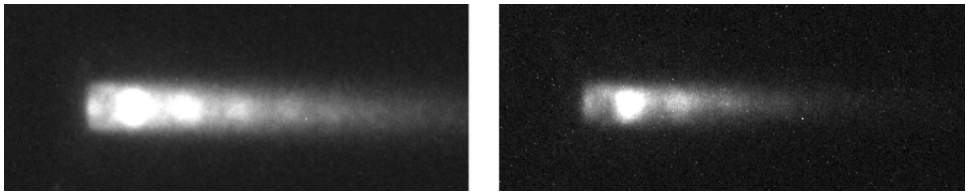

Fig. 3.7. Singular flame imaging results in separate phases of flow observed at same delay times. Initial conditions inside combustor changes overall flame timescales, posing difficulties in time matching intensified images.

Intensified imaging was an overall success, but there were several problems encountered when using the system. Due to the limitations of the ST-5 CCD, the picture frame rate is much greater than 1 second. This means that unlike the schlieren data, multiple phases of a single transient flame cannot be captured. Instead, single images can be taken of separate flames, and then stitched together to create an overall progression of the flame. However, the experiment is sensitive to initial conditions, and therefore the flame does not perform exactly the same way with each trial. For example, two pictures of separate flames obtained with the same delay time after ignition are shown in Figure 3.7. Although taken at the same delay time, they do not correspond exactly due to the minute flow differences within the experiment (i.e. solenoid timescales, turbulent interactions from A1 and A2, etc.). Therefore, intensified flame progressions are not considered. Instead, the examination will be limited to singular images of singular flames.

Lastly, varying the CCD exposure time and intensifier pulse time can give very different results. The methods for minimizing noise in the system, stated in Section 3.2, are demonstrated in Figure 3.8. The picture on the right is the result of a long exposure of the CCD coupled with a short pulse from the intensifier. The chemilluminescence of the flame is visible, but there is increased noise in the photo. Referring to Equation 3.3, a long exposure of the CCD will result in an increase

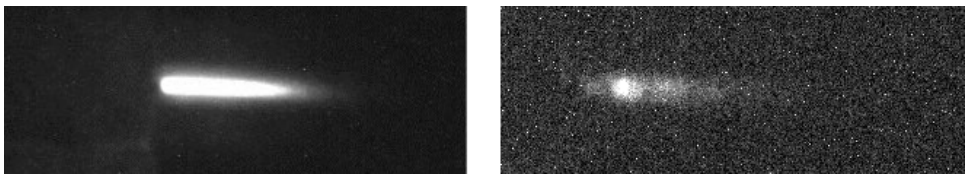

Fig. 3.8. Imaging difficulties using image intensifer. The left figure is an example of providing a large gate to the intensifier, resulting in a smeared photo with overexposed regions. The right figure the result of long exposure times of the CCD, causing increased noise in the image obtained.

of τ, $\dot{B}$, and $\dot{D}$, while keeping $\dot{P}$ the same. What results is an increase in noise, lowering the overall SNR of the system. The left picture is the result of increasing the gate width provided to the image intensifier. By doing so, a smearing effect is produced on the flame. All data regarding the supersonic jet structure is lost due to the increased gain of the photons emitted during combustion.

3.6 Schlieren Imaging

Light, when moving through a volume of air, will be refracted depending on the inhomogeneity in the density gradients and the resulting index of refraction [23]. Schlieren is a property of any transparent medium, including solids, liquids, and gases, which result from temperature changes, high speed flows, or the mixing of dissimilar fluids, amongst many other possible causes [23]. Essentially, density variations of some order (ρ, $\bigtriangledown\rho$, $\bigtriangledown^2\rho$) will produce visible streaks in a schlieren system [23]. Schlieren can provide an observer with a qualitative understanding of the complexities present in a flow. In the present work, the supersonic structure of the transient flame is observed using a schlieren setup, and is captured using a high speed camera.

The high speed cameras used in the schlieren portion of the results are the Casio EX-FH25 and the Fujifilm HS10, both of which render video at 1000 frames per

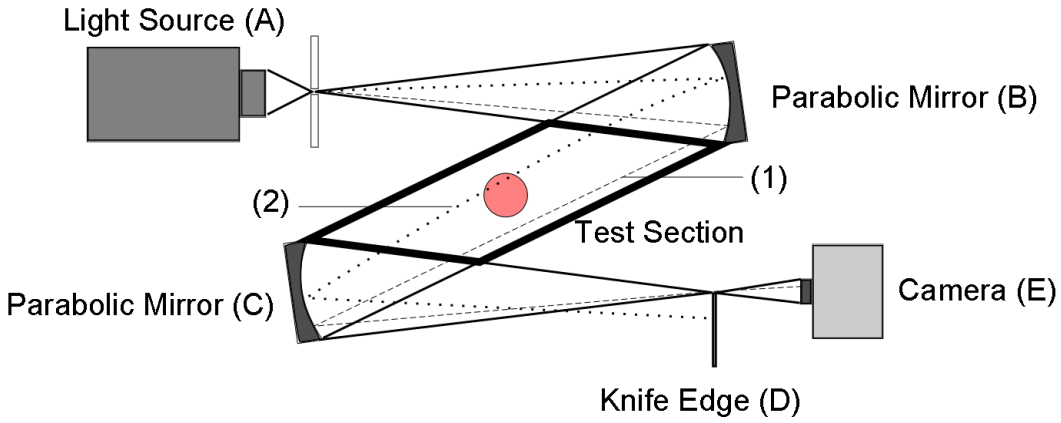

Fig. 3.9. Depiction of a Z-type schlieren setup. Light generated at (A) is focused onto the parabolic mirror (B). (B) collimates the light through the test section, arriving at the second parabolic mirror (C). (C) focuses the incoming light to a point at (D). The knife edge acts to block light rays that were refracted through the test section. Light ray (1) did not encounter an obstruction, and so passes through to the camera (E). Light ray (2) is refracted by the obstruction, and is consequently blocked by the knife edge at point (D).

second with a resolution of 224x64 pixels. This equates to one frame per millisecond, providing detailed views of the supersonic flow structure emanating from the combustor. Both cameras utilize a new complementary metal–oxide–semiconductor (CMOS) FPA. This new technology offers high speed imaging at a low cost.

There are several ways to construct a schlieren system, but the Z-type system was chosen due to its simplicity, as seen in Figure 3.9 [45]. The Z-type system utilizes two concave mirrors to collimate/decollimate the light rays. The system operates by first condensing light through a pinhole, which is then focused onto the first parabolic mirror (B). The mirror is located exactly 17.5 in away from the pinhole, causing the reflected light to be collimated. The collimated light is then focused by a second mirror (C) into a single point (D). At the focal point of the second mirror, a knife edge is used to cut off any light that is refracted due to gradients in the flow, as represented in Figure 3.9 by (2). The position of the knife edge is important, as it

controls which gradient directions will be amplified. In this experiment, due to the fast exposure times of the high speed cameras, a great deal of light was required to observe the transient flame. The light source utilized was a 150W fiber-optic haloid lamp condensed through a microscope lens.

The mirrors are angled at 8°, providing an incoming and outgoing beam angle of 16°. The Z-type schlieren system will always have some error in the focused beam due to astigmatism [23]. Astigmatism is the failure to focus a beam to a point, and results from symmetry breaking [23]. It should be noted that with the mirrors used in the Z-type system, any angle of the reflected light will produce astigmatic error. The problem cannot be rectified, by definition of the optical geometry. However, the abberations due to astigmatism are small and are not overtly visible in the gathered data.

4. RESULTS AND SUMMARY

In this chapter, results will be presented from the zero dimensional computation, schlieren imaging, and the ICCD. A relationship is made between the computational model and the schlieren high speed images. This is done by analysis of timescales within both systems. Additionally, flame properties are tracked through time and space using a Lagrangian reference frame. This allows flame properties to be analyzed just prior to the nozzle entrance. Flow properties through the nozzle are calculated using one dimensional isentropic flow relations. The calculation of thermodynamic properties downstream of the nozzle allow a comparison to be made between the schlieren images and the combustor model.

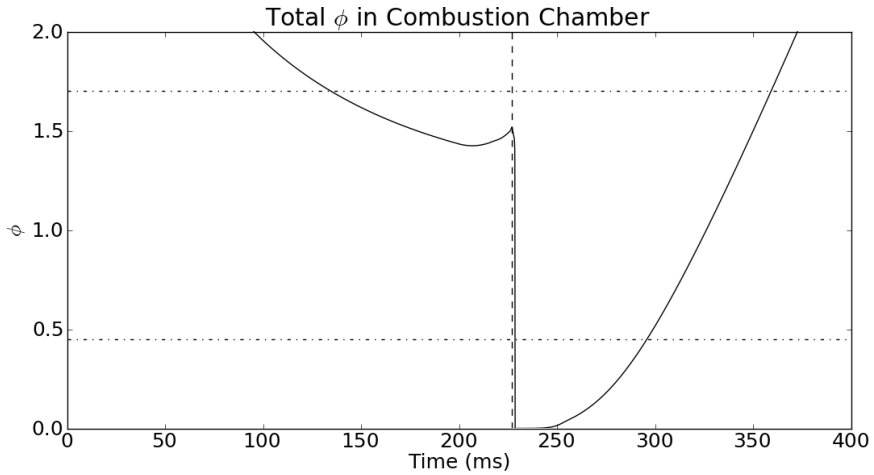

Fig. 4.1. Transient equivalence ratio in the combustor, computed using the zero-dimensional model. Horizontal dashed lines denote the upper and lower limits of flammability for methane in air [28]. The ignition point is at $t = 227$ ms, corresponding to a ϕ of approximately 1.5. The ignition delay is representative of experimental values, resulting in a small rise in equivalence ratio just prior to combustion.

4.1 Transient Zero-Dimensional Thermochemistry in the Combustor

Several timescales are important during the operation of the transient flame system. The process is initiated at $t = 0$ ms by opening the solenoid. The length of time that the solenoid is open is crucial in creating a flammable mixture for the system, as seen in Figure 4.1. The equivalence ratio ϕ is determined by the overall mass ratio of fuel and oxidizer in the combustor as it relates to the stoichiometric mass ratio. The fuel-air mass ratio in the chamber is dynamic, and is computed using the mass fractions reported by Cantera for each time step. When the experiment begins, the chamber is initially filled with methane, corresponding to an unbounded (infinite) equivalence ratio. Gradually, as air enters the chamber, the equivalence ratio will decrease until $t = 200$ ms. The equivalence ratio at $t = 200$ ms is based on the choked orifice values listed in Section 2.1 and corresponds to a local minimum of a transient case. If the calculation continued indefinitely, a steady state value of $\phi = 1.4$ would be reached.

At $t = 200$ ms, the solenoid begins to close. Ignition occurs at $t = 227$ ms. The lack of incoming air will result in ϕ increasing slightly, just prior to combustion. The 27 ms delay in ignition is needed in the experiment for gas mixing, but the WSR used by Cantera does not need this delay time. It is included in the simulation for ensuring as much possible continuity in the comparison between the experimental and simulated timescales. During combustion, the methane and oxygen are being consumed, causing the equivalence ratio to drop to zero. Because the methane continues flowing into the combustor and the solenoid is closed, the the lack of air in the system will create a second unbounded equivalence ratio at time $t \gg 250ms$.

When a flame is present, the fuel and oxidizer will be depleted, leading momentarily to $\phi = 0$. This duration between $t \approx 230$ ms and $t \approx 255$ ms, shown in Figure 4.1, shows the extent of the flame. Experimentally, the ignition point is determined by inspection of the flame, and audible cues. Ignition at a ϕ closest to one will result

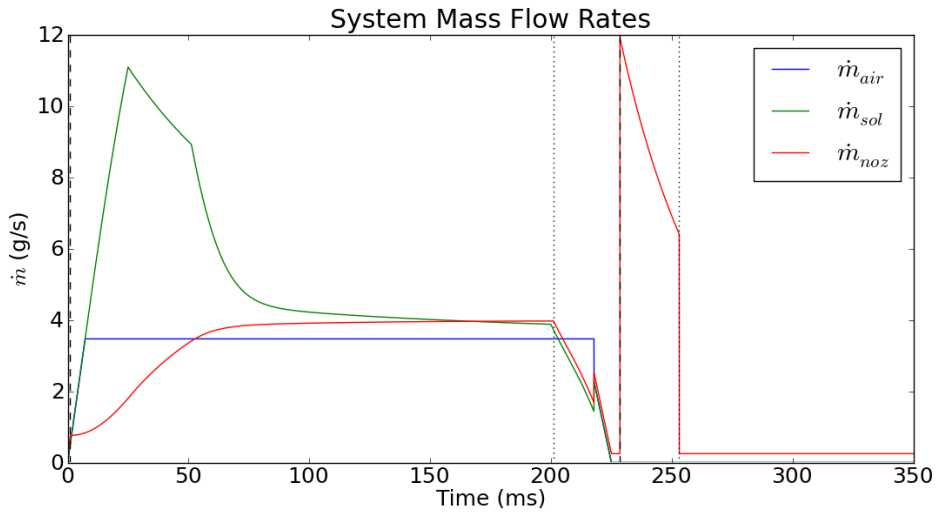

Fig. 4.2. The relative mass flow rates in the pressure system are calculated from Equations 2.2 and 2.4. They are based on several factors, including relative pressures, orifice areas, and choke conditions. Dashed lines represent the choked conditions for the nozzle. Dotted lines represent the transition from sonic to subsonic flow (unchoked) at the nozzle.

in the most vigorous combustion. Deviation from the optimal ignition point can still result in combustion, but it will result in a less intense flame.

The equivalence ratio in the system is based on the mass flow rates provided into and out of the WSR. As shown in Figure 4.2, the mass flow rates are computed at each time step using Equations 2.2 and 2.4 for the mass flow controllers that link each of the four pressure volumes, denoted as (1)-(4) in Figure 2.3. Initially, the mass flow rate through the nozzle ($\dot{m}_{noz}$) will be equal to the mass flow rate of methane ($\dot{m}_{fuel}$) because the nozzle is large enough to exhaust the small amount of incoming fuel, and because the solenoid is closed. When the solenoid opens, it will have a large area and mass flow rate ($\dot{m}_{sol}$) that is exhausting into the combustor, choking the nozzle. The pressure in the inertial volume will exhaust into the combustor transiently, until the pressure in the inertial volume is almost the same as the pressure in the combustion

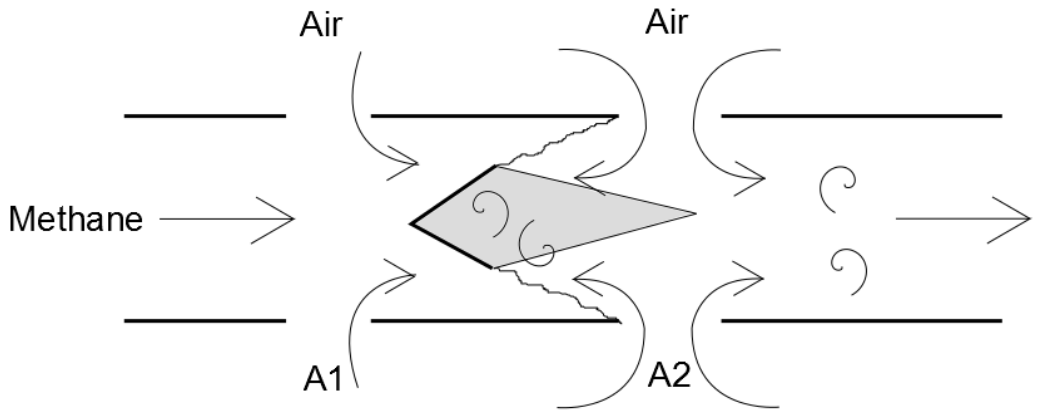

Fig. 4.3. Depiction of the possible mixing solution, allowing for a flammable mixture to be present at time of ignition.

chamber. When the inertial volume pressure lowers, the air orifice will become choked ($\dot{m}_{air}$), providing a constant mass flow rate until such time that the solenoid closes.

The interplay between all of the mass flow rates and volumes is performed by Cantera, where the choke conditions and mass flow rates are checked at each step, and updated for the next step. This allows a qualitative model to be produced based on simple assumptions, such as inviscid flow when subsonic, and isentropic flow when supersonic. The criterion for whether or not the nozzle chokes is based on the incoming mass flow rates for the system. If the incoming mass is lower than the outgoing mass, then the nozzle will not be choked. Additionally, if a large pressure and temperature increase occurs due to combustion, then the nozzle will choke. The two choke points are indicated in Figure 4.2 by dashed lines. In the same figure, the subsonic flow points are denoted by dotted lines.

One of the problems faced when implementing a zero-dimensional model is the assumption of perfectly mixed gases. The zero-dimensional model cannot capture gradients in space and mixing. When two gases are inserted into the reactor, the calculation considers them instantly and perfectly mixed. In a steady state calculation, this may not pose a problem. However, the transient behavior of the experiment is

heavily dependent on mixing time, implying that a mixing characteristic time must be accounted for. This mixing time was experimentally found to be approximately 27 ms. This means that in the experiment, the ignition is delayed after the solenoid is closed by approximately 27 ms. This is reflected in the simulation as well, although there are repercussions for delaying the ignition, as shown in Figure 4.1.

When the experiment is initiated, gas flows into the combustion chamber and is allowed to mix with the methane in the flame tube through areas A1 and A2, as shown in Figure 2.1. If the flow were to be acting in steady state, then the mixture would never ignite, due to the ratio of A1 and A2 and the metering orifice areas described. The equivalence ratio near the spark plug would exceed the limits of combustion, causing a failed ignition. However, the transient system ignites. This phenomenon can be explained due to the large turbulence effects generated by the flame holder boundary layer, and the sharp corners the flow encounters moving through A1 and A2. Figure 4.3 illustrates the turbulent mixing occurring near the flame holder. The flame holder provides a recirculation region in which the methane and air can mix, allowing for a flammable mixture to be created. Additionally, the swift movement of incoming air will result in an impinging jet through A1 and A2, causing more air to enter the recirculation region. For a brief moment, the mixture becomes flammable, but only in a transient configuration.

The graph in Figure 4.4 details temperature within the combustor as a function of time. The temperature remains relatively constant within the system until the ignition point at $t = 227$ ms. There is a minor temperature rise at $t \approx 40$ ms due to the sudden accumulation of mass in the combustion chamber. At ignition, the combustor temperature experiences a sharp increase due to chemical energy release. Because the air supply begins to decrease at $t = 200$ ms, the high temperature provided by reactions cannot be sustained with the diminishing oxygen levels. Therefore, the temperature within the combustor undergoes a decrease as the reactions cease to take place. What results is a gradual return to steady state, ambient levels ($t \gg 250$

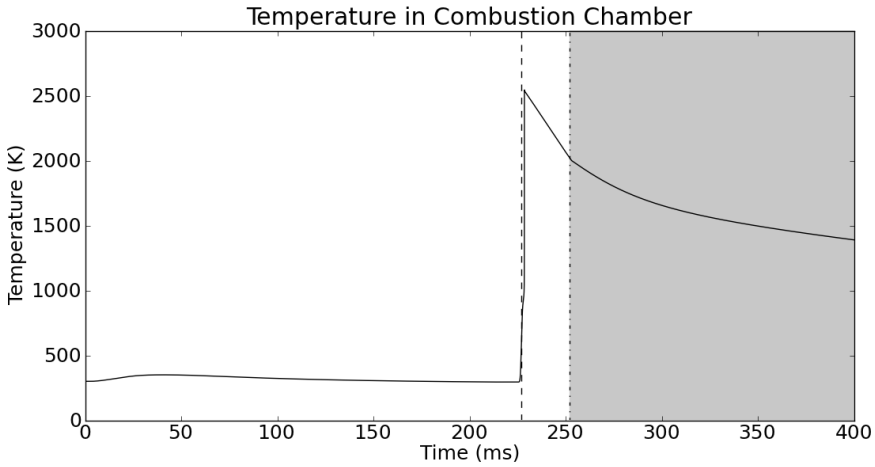

Fig. 4.4. Time evolution of the temperature profile within the combustor. The grayed-out portion relates to the time at which the flame parcel reaches the nozzle, exhausting out of the combustor.

ms) with no incoming air flow. Given enough time, the system would return to the exact state observed at $t = 0$ ms.

The chemistry of the flame can be quantified by analyzing the molecular makeup of the combustor gases as they change through time and space. Only major gas species are shown, although there are 53 different species used by the GRI-3.0 reaction mechanism. As discussed in Section 2.2, hydrogen atoms are used to ignite the flow, and are therefore extremely important in determining the state of combustion. The initial hydrogen addition is provided by a Gaussian pulse. This pulse reaches its maximum amplitude at $t = 227$ ms, attempting to mimick the ignition used in the experiment. The actual ignition time between the experiment and simulation will vary slightly, due to the methods in which they are each ignited. The experiment is ignited using a spark plug, which operates very quickly. However, igniting a flow in Cantera is done through hydrogen atoms, which will need time to react with the flow before providing combustion. This small reaction delay can be seen in Figure 4.5. The reaction delay in the simulation is approximately 1 ms.

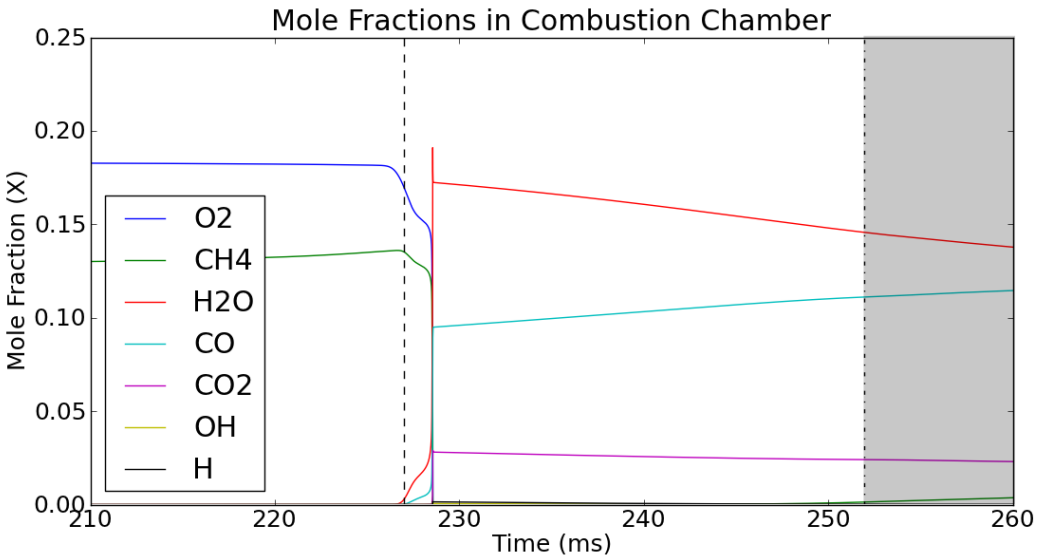

Fig. 4.5. Depiction of major mole fractions within the combustion chamber as a function of time. The rich flame ($\phi \approx 1.5$) will result in incomplete combustion, producing excess levels of CO. The dashed line indicates the maximum mass flow rate of pulsed hydrogen atoms ($\dot{m}_H$). Full reaction is observed approximately 1 ms after the maximum of the provided pulse. The grayed-out portion relates to the time at which the flame reaches the nozzle, exhausting out of the combustor.

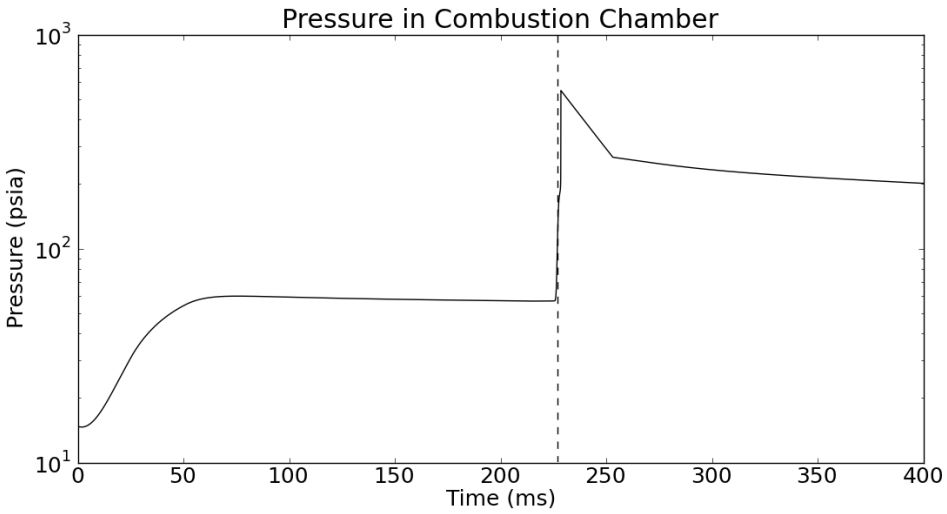

Fig. 4.6. Pressure within the combustion chamber. The sudden influx of air from the opening solenoid ($\dot{m}_{sol}$) at $t = 0$ ms will cause the pressure to rise in the combustion chamber. When combustion occurs, the pressure is drastically increased due to the energy release from the reaction.

The pressure profile within the combustion chamber in Figure 4.6 is tied very closely to the mass flow rates in Figure 4.2. When the solenoid begins to open at $t = 0$ ms, there is a large back pressure behind it. The nozzle in the combustion chamber is not initially choked, so the pressure within the chamber is atmospheric. The pressure difference across the solenoid will initially choke the solenoid orifice. Because the area of the solenoid is increasing when $t < 25$ ms, the mass flow rate ($\dot{m}_{sol}$) is also going to increase sharply. This sudden influx of air will choke the nozzle, resulting in accumulated pressure within the chamber. As the pressure in the inertial volume and the combustion chamber equalize, the upstream air orifice will choke, providing a constant mass flow rate ($\dot{m}_{Air}$) into the system, until the solenoid is closed. Soon after the solenoid closes, ignition occurs, creating a large pressure spike within the combustion chamber. The high pressure within the combustor will eventually be depleted through the nozzle ($\dot{m}_{noz}$).

4.2 Lagrangian Flame Progress

In order to link the transient zero dimensional model to experiment conditions, it is essential to account for the time the flame spends in the combustor before exiting the nozzle. If the time at which the flame exits the nozzle can be defined, then a direct comparison can be made between the simulation and the experiment regarding the temperature and flame composition downstream of the nozzle.

A convective timescale can be estimated by modeling the velocity of the flow within the combustor, and assuming a Lagrangian reference frame, as shown in Figure 4.7. The flow velocity will be a function of the system mass flow rate ($\dot{m}$), area of the flame tube A, and the density ρ of the system using a one dimensional model. The instantaneous flow velocity can be calculated at each time step using the following equation:

$$u(t') = \frac{\dot{m}(t')}{\rho(t')A} \tag{4.1}$$

where t' is a time variable, and u is the velocity in the chamber. The density of the flame parcel will be assumed constant as it moves through the combustor. This assumption will be examined at the end of this section, by comparing the relevant

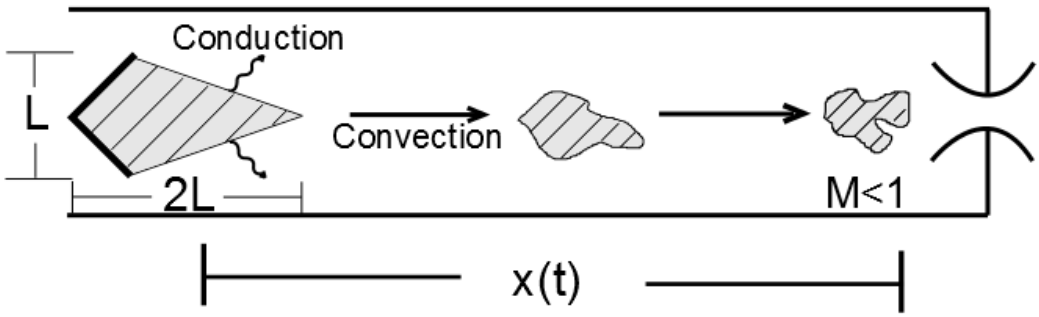

Fig. 4.7. Tracking of the flame parcel as it moves towards the nozzle. The heat loss from conduction is negligible compared to convective losses, allowing for estimation of values downstream of the nozzle.

timescales. By integrating the velocity equation with time, the distance that the fluid parcel moves can be computed:

$$x(t) = \int_0^t u(t')dt = \int_0^t \frac{\dot{m}(t')}{\rho(t')A}dt' \tag{4.2}$$

where $x(t)$ is the distance traveled by the fluid parcel. The distance d_{flame} required for the fluid parcel to travel from the ignition spark to the nozzle entrance is known from the geometry of the combustor. Therefore, by monitoring the value of $x(t)$ and t at each time step during the integration of Equation 4.2 and halting the calculation when $x(t) = d_{flame}$, the convective timescale of the model is found. The convective timescale for the simulation is calculated to be $t = \tau_2 \approx 25$ ms. This value agrees well with observed experimental values, as will be discussed in Section 4.4.

During the progression of the flame, it will be susceptible to heat loss from conduction through the combustor. The losses would complicate the model, as added heat loss effects are not currently considered in the simulation. Therefore, it is prudent to estimate whether the losses from conduction are prominent. If the flame can be convected to the nozzle faster than heat can be lost due to conduction, then the flame computed by the model can be directly linked to the experiment. The relative timescale of conduction can be approximated using dimensional analysis of thermal diffusivity (α). The units of α are m^2/s, indicating a need for a relative length scale (l) and a characteristic timescale (τ_c), and can be related as:

$$\alpha = \frac{l^2}{\tau_c} \tag{4.3}$$

The length scale can be determined using the geometry of the fluid volume (V) created by the flame holder, as shown in Figure 4.7. For the relatively low velocities within the combustor, this fluid parcel volume (V) can be estimated as a function of the flame holder geometry, in this case being obstruction height (L in Figure 4.7) [13]. This recirculation volume is based on experimental data compiled from Edelman,

and is estimated to extend approximately two obstruction heights downstream (2L in Figure 4.7) [13]. Therefore, the size of the fluid parcel volume is known. The length scale l for the thermal diffusivity can then be defined as $l \approx V^{1/3}$.

The Sutherland model can be used to approximate the thermal diffusivity of the fluid parcel as it undergoes combustion:

$$\frac{\alpha_{burn}}{\alpha_o} = (\frac{T}{T_o})^{1.7} \tag{4.4}$$

where α_o is the thermal diffusivity of the unburned gas, α is the high temperature diffusivity, T_o is the unburned temperature, and T is the temperature of the burning gas [46]. The thermal diffusivity of a gas α_o can be related to the kinematic viscosity ν_o as $\alpha_o \sim \nu_o$. Therefore, the Sutherland model can be used to estimate a thermal diffusivity for the high temperature fluid parcel. Using Equation 4.3 in conjunction with newly defined length scales l and the high temperature thermal diffusivity α_{burn}, the timescale τ can be estimated as:

$$\tau = \frac{V^{2/3}}{\alpha_{burn}} \tag{4.5}$$

Equation 4.5 provides an approximation of the characteristic diffusion (conduction) time through the fluid volume shown in Figure 4.7. The characteristic conduction time is calculated to be $\tau_c \approx 100$ ms.

The difference between the conductive timescale ($\tau_c \approx 100$ ms) and convective timescales ($t = \tau_2 \approx 30ms$) is very large ($\tau_c > \tau_2$). This means that the losses due to conduction will be negligible compared to the speed at which the flame is convected downstream to the nozzle. Therefore, conductive losses to the system may be disregarded and the density may be considered constant.

Equation 4.2 connects time from the WSR model to distance traveled from the ignition source in the experiment. With this relation, one may substitute distance for time in the simulation and obtain the results based on distance traveled, rather

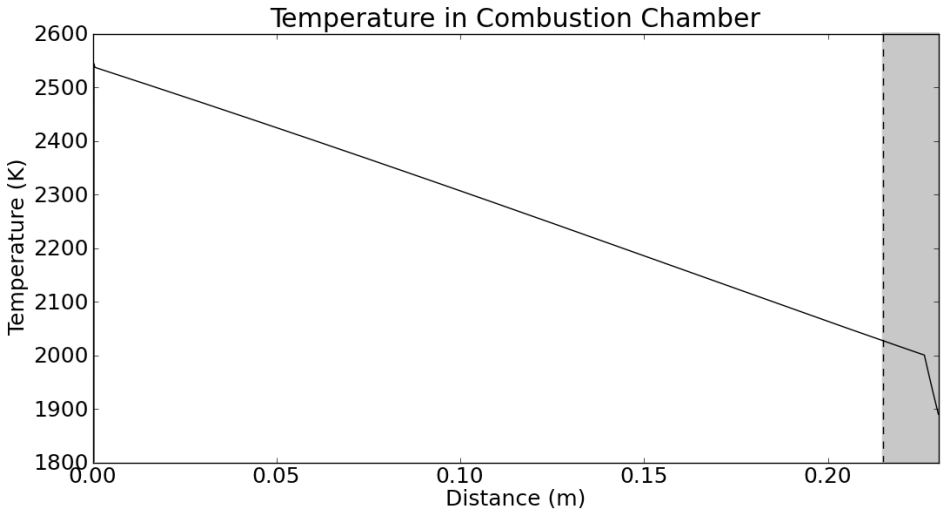

Fig. 4.8. Distance evolution of the temperature profile within the combustor. Zero distance corresponds to ignition at the flame holder. The grayed-out portion relates to the where the nozzle is located. This is the distance at which the flame reaches the nozzle, exhausting out of the combustor.

than time. Figure 4.8 details an example of this substitution, showing temperature change with distance as the flame parcel moves through the combustor towards the nozzle. The grayed-out areas indicate the point at which the flame parcel reaches the nozzle, both temporally and spatially, and should be considered as the point at which the flame exits the combustor. Therefore the data past this point should not be considered. The downward slope of the temperature indicates that the flame is cooling down before it gets to the nozzle. This is caused by several reasons. The pressure in the combustor is dropping drastically at this point, which will lower the other parameters inside the combustor, based on the ideal gas law. Additionally, the flame is reacting while moving towards the nozzle. The reaction began very rich, so it will not be able to sustain reaction. Therefore, the flame will not be able to provide enough energy to keep the temperature up. This can be seen in Figure 4.9. The chemical composition of the flame is also changing through space. The rich flame is

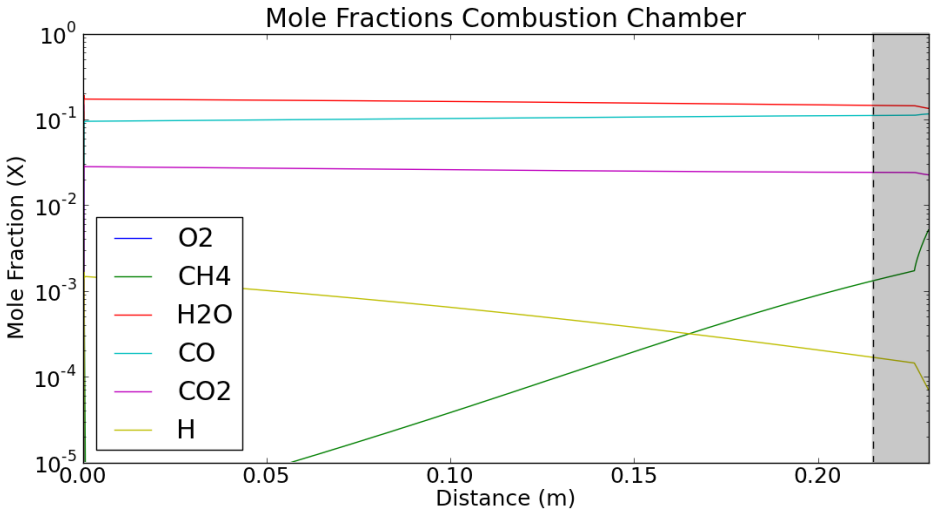

Fig. 4.9. Depiction of the mole fractions throughout combustion as distance traveled by the flame. Zero distance corresponds to ignition. The grayed-out portion relates to the where the nozzle is located. This is the distance at which the flame reaches the nozzle, exhausting out of the combustor.

starting to extinguish when it reaches the nozzle, shown by the increase in methane. If the reaction were still taking place, the methane would be in the process of being consumed. Because it is rising, the reaction must be slowing down.

One shortcoming of using the Lagrangian approach within a WSR lies in the idea of the flame parcel being an "open system". If the fluid parcel were truly moving in the combustor with speed equal to the surrounding flow, outside gases would not be entering the parcel, as is indicated in Figure 4.9. However, if considered for qualitative purposes it is applicable to the experiment. The ability to connect the timescales of the experiment to the WSR is valuable information, as it can be applied to many other simulations. Transforming a zero-dimensional model into a one-dimensional model is especially useful for transient problems, as it can help to describe the properties of a system as it evolves through space, and not just time.

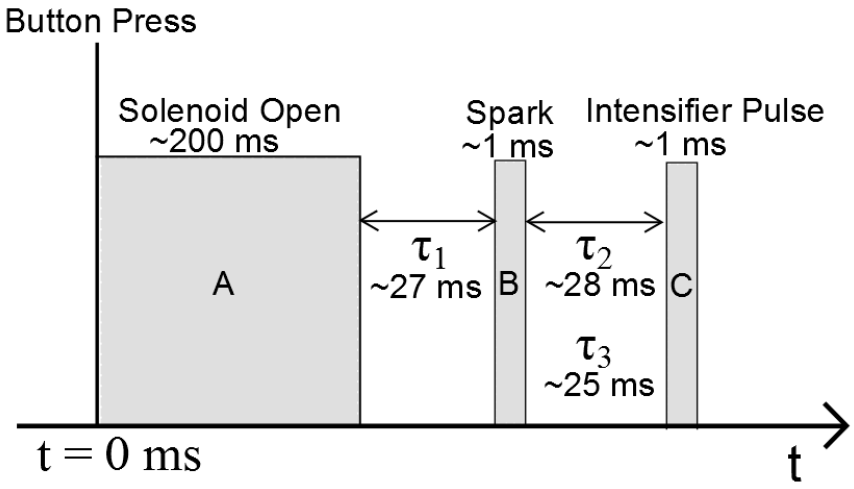

Fig. 4.10. Relative timescales used in the experiment. (A) represents the open solenoid time (∼200 ms), (B) is the ignition spark (∼1 ms), and (C) is the duration of activation of the image intensifier (∼1 ms). τ_0 is the initiation of the experiment, signified by a button press. The first delay (τ_1) determines the ignition point, and the second delay (τ_2) determines which phase of the flame is captured. τ_3 is from the Lagrangian approximation and corresponds to τ_2.

Finally, Figures 2.2 and 3.6 can be updated to include the newly calculated travel time of the simulated flame, as shown in Figure 4.10. This value corresponds directly to the delay set by the ICCD. Experimentally, the flame travel time is found to be 28 ms, as indicated in Figure 4.10 by τ_2. The Lagrangian approximation calculates the flame travel time to be 25 ms (τ_3), providing good correlation between the simulation and the experiment.

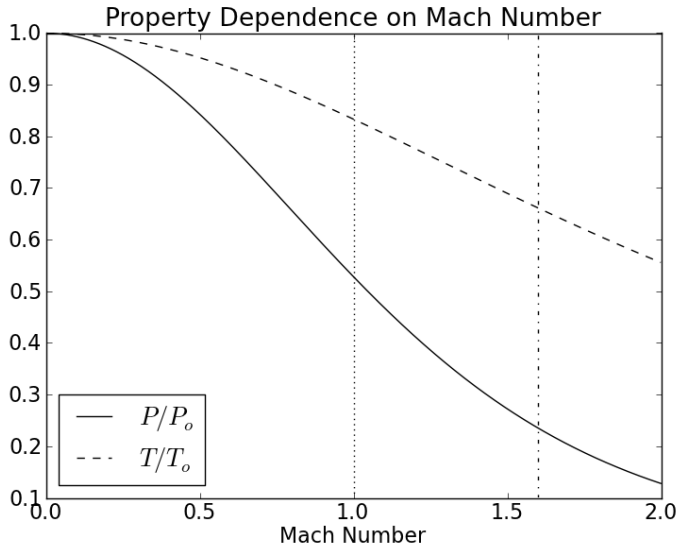

Fig. 4.11. The flow properties depend directly on the Mach number of the flow. Critical points are dictated by the values at $M = 1$. If the pressure ratio at the critical point is exceeded, the flow will become supersonic ($M > 1$) downstream of the nozzle throat. Nozzle geometry dictates an exit Mach number of 1.6, giving known values for temperature and pressure at the nozzle exit.

The regime for nozzle flow can be determined using Equation 2.3. If the ratio of downstream (atmospheric) pressure to upstream (combustor) pressure does not reach the critical value described by Equation 2.3 at the nozzle throat, then flow downstream of the nozzle throat will remain subsonic. Conversely, if the critical pressure is reached, then the Mach number at the nozzle throat will be $M = 1$, resulting in a maximum nozzle mass flow rate ($\dot{m}_{nozzle}$). Figure 4.11 details the downstream (nozzle exit) to upstream (combustor) pressure and temperature ratios at specified Mach numbers for a constant specific heat ratio γ relating to air. The critical pressure ratio is described by the ratio at $M = 1$. If the ratio of atmospheric pressure to combustor pressure is less than the critical pressure ratio, then the flow

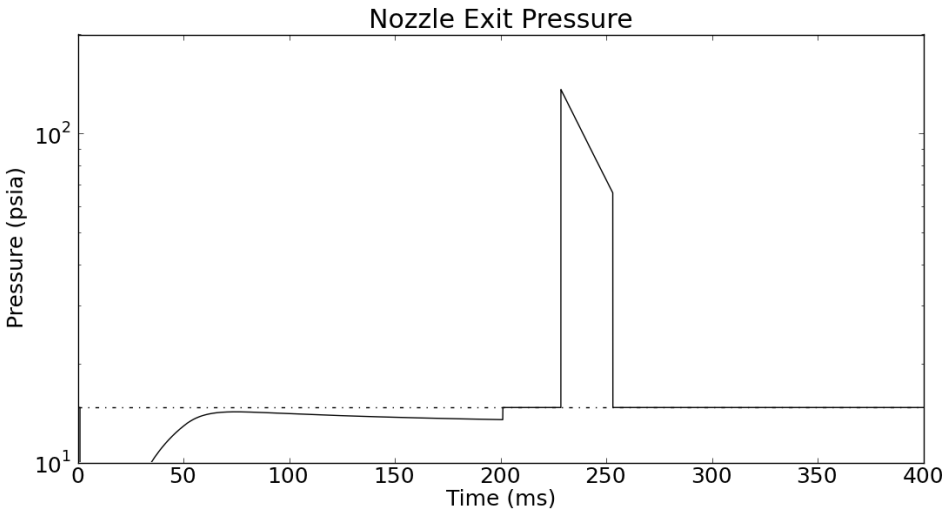

Fig. 4.12. Computed pressure at the nozzle exit during transient flame simulation. The discontinuity at $t \approx 230$ ms and $t \approx 255$ ms is the result of switching between subsonic and supersonic flow regimes. The initial choked behavior ($t < 200$ ms) corresponds to an overexpanded jet. The pressure rise from combustion creates an underexpanded jet at nozzle exit. A brief region of subsonic flow is observed between 200 ms $< t <$ 230 ms. The dashed line represents atmospheric pressure.

will reach supersonic speeds past the nozzle throat. It is assumed that due to the small size of the nozzle used in the experiment there will be no shock waves present in the nozzle. Additionally, isentropic flow can be assumed if the expansion process is both adiabatic and reversible [2]. Therefore, once the supersonic regime is obtained downstream of the nozzle throat the pressure and temperature at the nozzle exit will be dependent entirely on the combustor conditions. In the case of subsonic flow, it is assumed the exit pressure and temperatures are approximately equal to the ambient conditions downstream of the nozzle.

The expansion of a flow through a choked nozzle can be assumed isentropic (ds = 0) in the absence of strong waves or reaction. It is assumed, based on the size and contour of the nozzle, that there will be no separation within the nozzle, and

therefore no shock waves. For this model, it is also assumed that the chemistry of reaction is frozen through the nozzle [14]. This approximation ensures there is no entropy change due to reaction within the flow. These assumptions allow one dimensional isentropic equations to be used to predict the values for temperature and pressure at the nozzle exit. The pressure at the nozzle exit is shown in Figure 4.12. Pressure and temperature are determined using the one dimensional isentropic nozzle equations:

$$\frac{P}{P_o} = (1 + \frac{\gamma - 1}{2} M^2)^{\frac{-\gamma}{\gamma - 1}} \tag{4.6}$$

$$\frac{T}{T_o} = (1 + \frac{\gamma - 1}{2} M^2)^{-1} \tag{4.7}$$

where P_0 is the chamber pressure, P is the nozzle exit pressure, T_o is the temperature in the combustor, which is assumed at stagnation conditions, and T is the nozzle exit temperature [2]. The exit Mach number is known from Section 2.1, and γ is computed at each time step by Cantera. The initial choked condition from Figure 4.2 results in a combustor pressure that is slightly less than 4 atmospheres. When isentropically expanded using Equation 4.6, the pressure at the nozzle exit will be slightly lower than atmospheric. This is characteristic of an overexpanded jet. Ideally, a nozzle is most efficient when $P_{exit} = P_{atmospheric}$. When $P_{exit} < P_{atmospheric}$, the jet is overexpanded by the nozzle. Conversely, if $P_{exit} > P_{atmospheric}$, the jet is not expanded enough, or underexpanded.

Figure 4.12 details the exit pressures calculated in the simulation. As discussed, the nozzle will choke very early in the simulation. What results is an overexpanded jet during the first choked region, until $t \approx 200$ ms. When the solenoid begins to close, the incoming mass flow rates to the combustor ($\dot{m}_{sol}$ and $\dot{m}_{fuel}$) cannot sustain the choked condition, and so the nozzle will become subsonic. This is indicated in the figure from $t = 200$ ms to $t \approx 230$ ms. Since the flow is ignited at $t = 227$ ms, the pressure and temperature in the combustion chamber will rise dramatically, as calculated by Cantera in Figures 4.4 and 4.6. The conditions experienced by

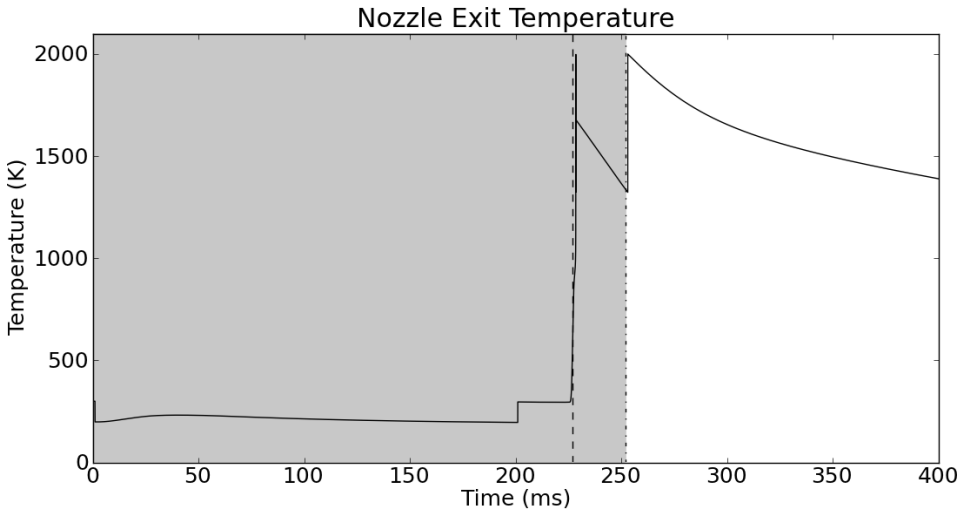

Fig. 4.13. Computed temperature at the nozzle exit during transient flame simulation. The greyed-out region pertains to temperatures not observed at the nozzle due to the convective timescales within the combustor. The discontinuity at $t = 255$ ms is the result of switching from a supersonic regime to a subsonic regime, as described by Equation 4.7.

the combustor during reaction will choke the nozzle a second time, resulting in an underexpanded jet, calculated from the isentropic flow relations. As the temperature and pressure of the system is quickly exhausted through the nozzle, the nozzle will no longer be choked, resulting in atmospheric exit pressures ($t > 255$ ms). The discontinuity in the pressure profile is from the sudden transformation of a subsonic flow to a supersonic flow. Although in reality this transition would be a smoother curve as the flow would need time to accelerate, it would still be a relatively fast transition. Therefore, it is a good approximation of the transformation from subsonic to supersonic flow.

The same assumptions used in calculating the nozzle exit pressure also apply to calculating temperature. The temperature at the nozzle exit can therefore be computed using Equation 4.7. The grayed-out portion of the nozzle exit temperature profile in Figure 4.13 is data not observed in the experiment, because the flame

parcel has not yet reached the nozzle. Therefore the temperatures calculated before this time will not be observed experimentally. The temperature computed at the exit is based directly on the combustor temperature. As discussed already, the zero dimensional model that is used to compute the reactor is transformed using Lagrangian particle tracking. In this work, the assumption is made that the flame parcel exiting the combustor will have properties very close to the one predicted by the program.

Figure 4.13 depicts is the simulated temperature profile at the nozzle exit based solely on the combustor temperature, and the choked condition. The discontinuities at $t = 228$ ms and $t = 255$ ms are from the instantaneous switching of a subsonic to supersonic regime, and from a supersonic to subsonic regime, respectively. When the nozzle is not choked, the nozzle exit temperature is approximated as the combustor temperature. When the flow is choked, the exit temperature is calculated using Equation 4.7.

It is also important to note that pressure will act quickly within the combustor, and temperature will have the effect of a delay based on the timescale found in Section 4.2. Pressure is distributed through the combustor using pressure waves which travel at the speed of sound. Temperature, however, is communicated through diffusion, conduction, convection, etc. The temperature "flowing" through the combustor will be mainly dictated by the convection, or fluid velocity, within the combustion chamber. The pressure, however, can be assumed within the model to be acting on the nozzle immediately.

4.4 Supersonic Flame Behavior

A supersonic flow downstream of a nozzle will have a defined structure at the nozzle exit based on gas dynamics, and can be seen in Figures 4.14 and 4.15. An overexpanded jet is observed when the pressure at the nozzle exit is less than the surrounding atmospheric pressure [2]. What results is a series of diamond patterns

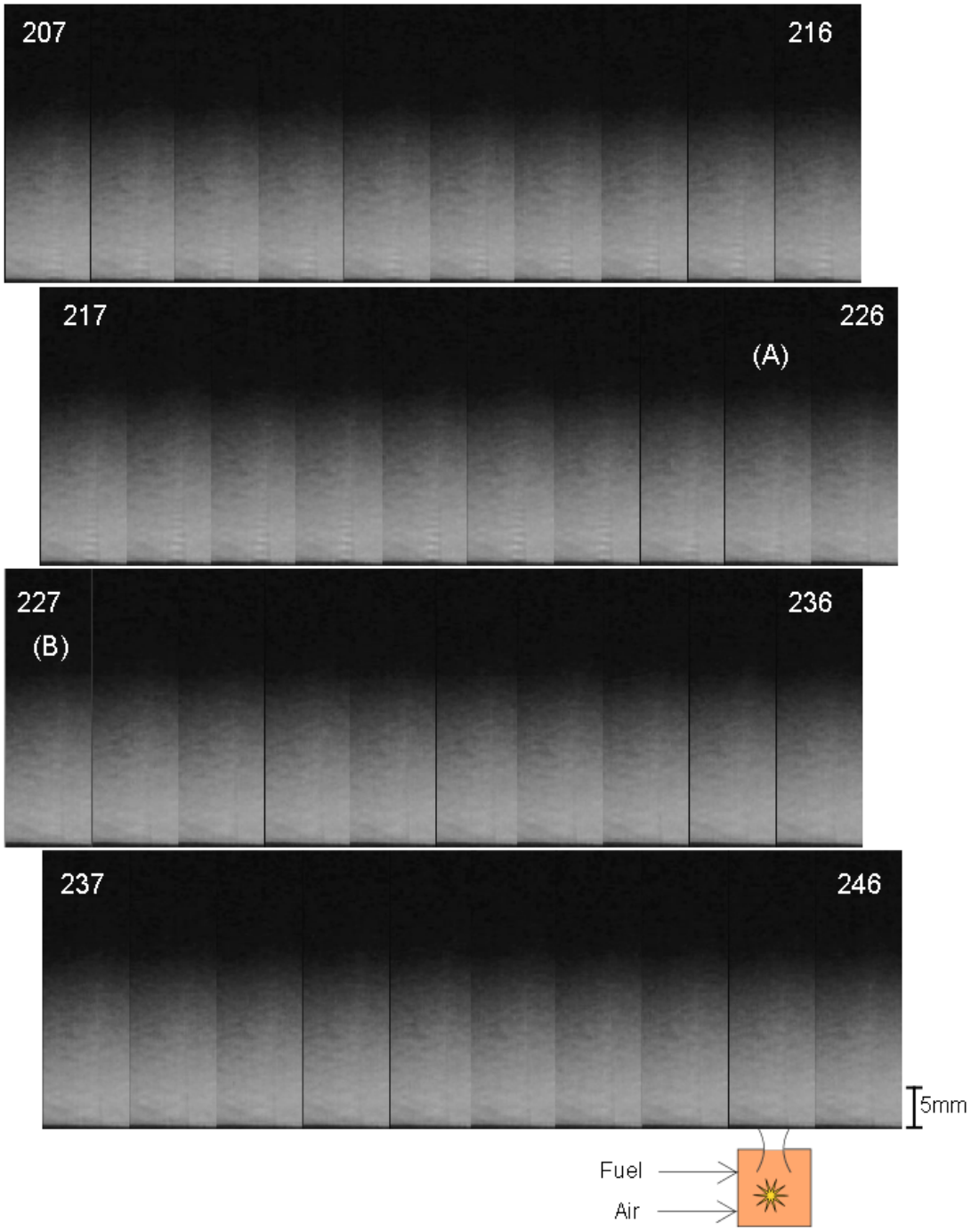

Fig. 4.14. Transient flame experiment captured by a high speed camera in conjunction with a schlieren system. (A) - Solenoid fully closed. (B) - Ignition.

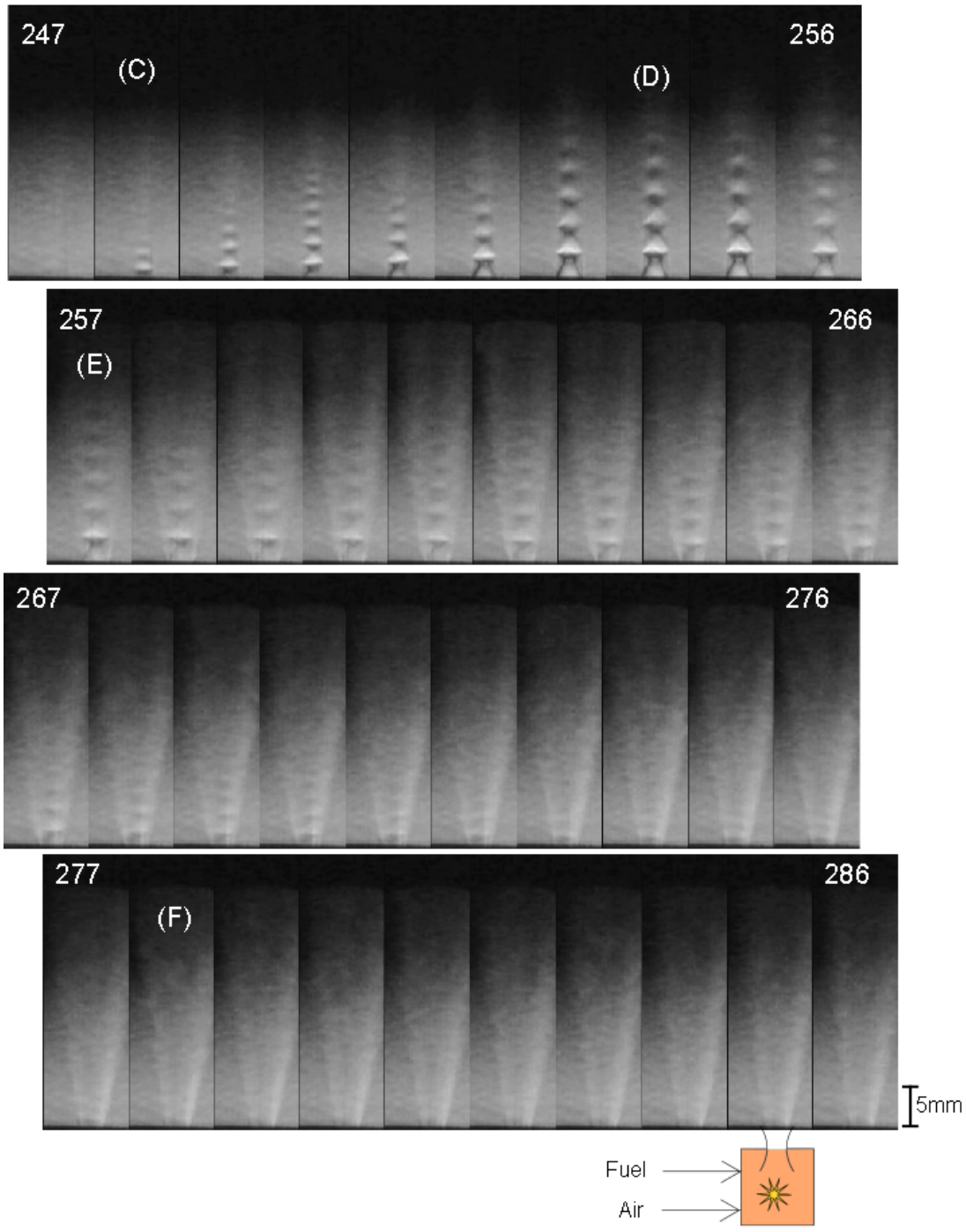

Fig. 4.15. Continued schlieren system imaging. (C) - Flame begins to emerge from nozzle. (D) - Most vigorous flame. (E) - Entrainment begins. (F) - Jet becomes subsonic.

caused by shock wave interactions in the flow. The shock waves form when the supersonic flow meets the free boundary of a quiescent flow. Because pressure across the boundary must be conserved, an oblique shock wave will form at the exit. These oblique shocks emanate from all points of the nozzle circumference, eventually meeting at the centerline of the flow. At this point they will reflect, hitting the free boundary. The new reflection will consist of expansion fans, which will behave in a similar fashion, continuing the diamond pattern until coalescing into oblique shocks once more. This pattern will continue until enough energy is lost and the flow becomes subsonic at all points [2]. An underexpanded jet will have a similar shockwave structure, only the process will begin with expansion fans, which will reflect into oblique shock waves. For this experiment, an inviscid, isentropic flow model is assumed.

Figures 4.14 and 4.15 detail the results of the schlieren experiment using the high speed CMOS camera. As discussed in Section 2.1, the CMOS camera frame rate is 1000 Hz, providing one frame per millisecond. The camera used does not possess the ability to be triggered. This complicates the analysis of the transient flame because there is no set starting point to the data. Therefore, the task of analyzing the data falls entirely on the interpretations of the experimenter. Through examination of the images, the following events were found. Prior to (A) in Figure 4.14, the flow is overexpanded, resulting in very small shockwave interactions. At (A), the solenoid is fully closed, allowing the nozzle to stop choking. Ignition occurs at (B), beginning the convection of the flame through the combustor. As described in Section 4.2, the flame will require a convective time to reach the nozzle. The flow remains subsonic through the nozzle until (C) in Figure 4.15. At (C) the flame is beginning to emerge from the combustor, and the nozzle is choked. (D) shows the most vigorous point of the flame, manifested as an underexpanded jet. At (E), the high speed, high temperature flow begins to entrain surrounding fluid, causing a “sheathing” effect

around the supersonic jet. Finally, at (F) the nozzle stops being choked, and resumes subsonic flow once more.

Points (A)-(F) are identified through the use of the ICCD, which is the only piece of equipment available for the experiment that can provide a link between the schlieren images and the timescales described in Figure 4.10. Because the ICCD is precisely timed, the delay time between ignition and flame emergence is known. This information can allow for a "time stamp" to be made on the schlieren images. It is known that the ignition point of the system occured 27 ms before the emergence of the flame. Therefore, the ignition point should be located in Figure 4.14, around point (B). It is also known that the solenoid, assuming a 25 ms closing time, should be closed around point (A).

The results computed through Cantera can also aid in correlating the schlieren image data. The frames of the schlieren images are numbered to represent the link between the simulation and the experiment, i.e. the simulated system is ignited a $t = 227$ ms reflected in the schlieren images at (B), frame 227. The modeled combustion system indicates that the flow will be choked until the solenoid is closed. Careful analysis of the schlieren frames reveal a shock wave pattern occurring at a much smaller scale prior to (A). This is clearly the result of a choked nozzle. This must correspond to the first region of choked flow from the solenoid orifice, as shown in Figure 4.6. Frames between (A) and (C) do not show any evidence of choking. This is because the solenoid valve has closed, and it is assumed fully closed by (A), as it is in the model. This gives very good agreement between the empirical data gathered by the schlieren system, and the qualitative simulation. The simulation predicts that the second choked region should last for approximately 25 ms. Examining Figure 4.15, the strong underexpanded jet and shock pattern can be observed from (C)-(F). This means the experimental choked region lasted for approximately 30 ms, whereas the simulation estimates a choked region of 25 ms. Qualitatively, the Cantera model of the transient pressure system applies well to the experiment.

The "sheathing" flow structure developed at (E) is the shear layer due to the entrainment of the surrounding flow. The transient jet beginning at (C) is occurring so fast that the entrainment of the surrounding flow cannot match the speed of the jet. When the jet is initially observed, there is little to no entrainment of surrounding fluid. However, when the high pressure jet emerges from the nozzle, there is an approximate 9 ms delay before the surrounding fluid becomes entrained. Past work, for example [47–49], indicates that transient, pulsed jets exhibit stronger entrainment than their steady state counterparts. Future work will examine this premise by eliminating ignition, and comparing the resulting shear layer development. The schlieren photographic evidence seems to suggest a suppression of entrainment from the ambient. In fact, reduced entrainment is an effect of compressibility in supersonic shear layers [50–52]. The compressibility and the associated strong waves lead to lower growth rates [52], which in turn signify lower entrainment.

Even more important than the compressibility effect is the presence of combustion for lowering entrainment. Turbulent jet flames exhibit a decrease in entrainment that has been well documented in numerous studies (e.g. [53,54]). For example, the study in reference [53] measured a reduction of up to 30% in the rate of entrainment due to the presence of burning. When compressibility and reaction are combined, as is the case in supersonic flames, the entrainment is expected to be further reduced, and the growth rate of the shear layer is severely impeded [55–57]. The present flame includes all three effects, and the synergy between them is difficult to predict.

Figure 4.16 demonstrates the best photo gathered by the newly constructed ICCD, with a comparison to one of the observed schlieren frames. The chemiluminescence of the flame is captured, and is amplified for ease of viewing. Several important facts can be taken from this image. The chemillumescence of the flame is clearly visible, indicating a chemically reacting flow present downstream of the nozzle. Combustion occurs in the regions of subsonic flow within the jet. These areas are identified by their high photon generation rate. Additionally, the structure

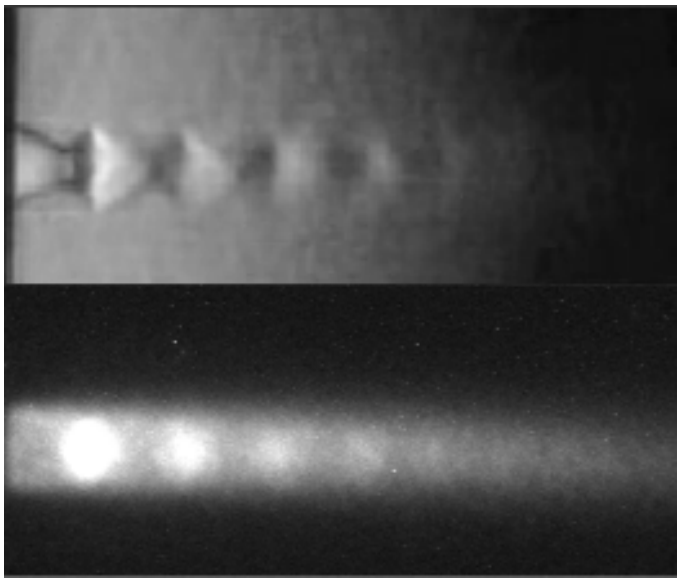

Fig. 4.16. Ideal intensified image of transient flame. Background noises are minimized, causing flow structure and chemiluminescence to be more easily observed. A direct comparison can be made between the length scales of the schlieren and intensified images.

of the jet is comparable to the gathered schlieren images. Although solid boundaries cannot be seen, the bright areas are comparable to the diamond patterns in Figure 4.15.

The ICCD was capable of determining the flame emergence from the nozzle. While the schlieren setup would only give information regarding the overall density gradients of the flow, chemiluminescence of the flame can be observed with the ICCD. This means that even if there is a supersonic shock wave structure, it may not necessarily be a flame. Because the ICCD is a triggered (gated) system, it can be used to identify the flame emergence, and track its progress in space. This was useful in comparing the model results to the experiment, as relations between distance and time in Section 4.2 were made based on the timescales observed in the experiment. The transient flame itself suffers from reproducibility based on the initial conditions in the combustor, and the timing variations of the mechanical components used in

the experiment. However, averaged data from multiple photos can be used to specify the timing of the flame.

4.5 Summary

In this thesis, an experiment was designed and constructed to produce a transient, supersonic methane/air flame. The transient effect was produced using an electromagnetic solenoid to pulse air into the combustor. Various experimental timescales were discussed. To image the emerging flame front, a newly designed ICCD was constructed. The creation of the ICCD necessitated the construction of a high voltage power supply, and an optical relay system to couple the image intensifier to a CCD. Additionally, a z-type schlieren system was constructed to gather high speed video information of the transient flame. The thermodynamic properties of the system were quantified computationally using Cantera. Pressure, temperature, and chemical composition were discussed as they evolved with time through the combustor. The results showed good agreement between observed experimental data and the computational model. A comparison was made between the schlieren data from the experiment and the computational model. Finally, ICCD imaging was used to observe the chemiluminescence of the flame, and to help tie the timescales of the experiment to the simulated model.

4.6 Future Work

Immediate work will focus on analyzing changes to the combustion process through variance of initial conditions. Further research on modifying the timescales of the experiment will be completed by adjusting the open solenoid time and ignition point of the system. The results obtained from this will increase the understanding of how the equivalence ratio in the combustion chamber is affected by different timescales. Furthermore, there is insufficient data to fully explain the significance of the area

ratios A1 and A2 from Figure 2.1. Multiple tests can be constructed to explain this problem. Two immediate experiments will focus on changing the area ratio, and changing the distance between A2 and the ignition point. By changing the position of A2, understanding the limits of recirculation in the chamber can be achieved. Experiments using an underexpanded nozzle will also be performed. By changing the nozzle dimensions, an underexpanded jet can be created, changing the pressure and temperature profiles. Additionally, the flow structure will change significantly. The simulated model can also be improved through the addition of heat loss effects. By adding heat loss to the system, a more complete and accurate description of the transient flame event can be considered. Lastly, immediate work will include joining the high speed CMOS camera to the image intensifier relay. As of now, the CCD may prove insufficient for analyzing the time dependent properties of the flow. By increasing the overall system gain with the image intensifier, higher quality schlieren videos can be obtained.

Long term future work will include laser diagnostics, and building multiple combustor units for jet interaction. Planar laser induced fluorescence (PLIF) can provide quantifiable measurements of the flame constituents. As of now, relying on the computed chemistry data alone is insufficient for truly understanding the transient flame. PLIF can provide the detailed flame chemistry, allowing for further comparison of the experiment to the simulation. Additionally, the ultimate goal is to produce a system which forces the interaction of the supersonic jets. This will require the construction of several transient combustors for use in synchronization. The overall assembly of the experiment will require accurate timing, further complicating system parameters.

REFERENCES

[1] Fry, R., "A Century of Ramjet Propulsion Technology Evolution," *Journal of Propulsion and Power*, Vol. 20, No. 1, 2004, pp. 27–58.

[2] Anderson, J., *Modern Compressible Flow*, 3rd ed., McGraw-Hill, 1982, pp. 120–145.

[3] Kloesel, K. J., Ratnayake, N. A., and Clark, C. M., "A Technology Pathway for Airbreathing, Combined-Cycle, Horizontal Space Launch Through SR-71 Based Trajectory Modeling," 17th AIAA International Space Planes and Hypersonic Systems and Technologies Conference, San Francisco, CA, AIAA Paper 2011-2229, Apr. 2011.

[4] Roy, G., Frolov, S., Borisov, A., and Netzer, D., "Pulse Detonation Propulsion: Challenges, Current Status, and Future Perspective," *Progress in Energy and Combustion Science*, Vol. 30, May 2004, pp. 545–672.

[5] Yan, Y., Fan, W., Wang, K., Zhu, X., and Mu, Y., "Experimental Investigations on Pulse Detonation Rocket Engine with Various Injectors and Nozzles," *Acta Astronautica*, Vol. 69, 2011, pp. 39–47.

[6] Milton, B. and Pianthong, K., "Pulsed, Supersonic Fuel Jets – A Review of Their Characteristics and Potential for Fuel Injection," *International Journal of Heat and Fluid Flow*, Vol. 26, 2005, pp. 656–671.

[7] Zakrzewski, S., Milton, B., Pianthong, K., and Behnia, M., "Supersonic Liquid Fuel Jets Injected into Quiescent Air," *International Journal of Heat and Fluid Flow*, Vol. 25, 2004, pp. 833–840.

[8] Cutler, A., "High-Frequency Pulsed Combustion Actuator Experiments," *AIAA Journal*, Vol. 49, No. 9, Sept. 2011.

[9] Giuliani, F., Lang, A., Gradl, K., Siebenhofer, P., and Fritzer, J., "Air Flow Modulation for Refined Control of the Combustion Dynamics Using a Novel Actuator," *Journal of Engineering for Gas Turbines and Power*, Vol. 134, Feb. 2012.

[10] Gilarranz, J., Traub, L., and Rediniotis, O., "A New Class of Synthetic Jet Actuators – Part I: Design, Fabrication and Bench Top Characterization," *Journal of Fluids Engineering*, Vol. 127, Mar. 2005, pp. 367–376.

[11] Lefebvre, A., Ibrahim, A., and Benson, N., "Factors Affecting Fresh Mixture Entrainment in Bluff-Body Stabilized Flames," *Combustion and Flame*, Vol. 10, 1966, pp. 231–239.

[12] Longwell, J., Frost, E., and Weiss, M., "Flame Stability in Bluff Body Recirculation Zones," *Industrial & Engineering Chemistry*, Vol. 45, No. 8, 1953, pp. 1629–1633.

[13] Edelman, R. and Harsha, P., "Laminar and Turbulent Gas Dynamics in Combustors - Current Status," *Progress in Energy and Combustion Science*, Vol. 4, 1978, pp. 1–62.

[14] Sutton, G. and Biblarz, O., *Rocket Propulsion Elements*, 8th ed., John Wiley & Sons, New Jersey, 2010, pp. 57–63.

[15] Hill, P. and Peterson, C., *Mechanics and Thermodynamics of Propulsion*, 2nd ed., Addison-Wesley Publishing Company, 1992.

[16] Ehn, A., Johansson, O., Bood, J., Arvidsson, A., Li, B., and Alden, M., "Fluorescence Lifetime Imaging in a Flame," *Proceedings of the Combustion Institute*, Vol. 33, 2011, pp. 807–813.

[17] Dam, N., Rodenburg, M., Tolboom, R., Stoffels, G., Huisman-Kleinherenbrink, P., and ter Meulen, J., "Imaging of an Underexpanded Nozzle Flow by UV Laser Rayleigh Scattering," *Experiments in Fluids*, Vol. 24, 1998, pp. 93–101.

[18] Docquier, N., Belhalfaoui, S., Lacas, F., and Darabiha, N., "Experimental and Numerical Study of Chemiluminescence in Methane/Air High-Pressure Flames for Active Control Applications," *Proceedings of the Combustion Institute*, Vol. 28, 2000, pp. 1765–1774.

[19] Ikeda, Y., Kojima, J., and Hashimoto, H., "Local Chemiluminescence Spectra Measurements in a High-Pressure Laminar Methane/Air Premixed Flame," *Proceedings of the Combustion Institute*, Vol. 29, 2002, pp. 1495–1501.

[20] Katanoda, H., Miyazato, Y., Masuda, M., and Matsuo, K., "Pitot Pressures of Correctly-Expanded and Underexpanded Free Jets from Axisymmetric Supersonic Nozzles," *Shock Waves*, Vol. 10, 2000, pp. 95–101.

[21] Tabei, K., Shirai, H., and Takakusagi, F., "Density Measurements of Underexpanded Free Jets of Air from Circular and Square Nozzles by Means of Moiré-Schlieren Method," *JSME International Journal*, Vol. 35, No. 2, 1992.

[22] Tkacik, P., Keanini, R., Srivastava, N., and Tkacik, M., "Color Schlieren Imaging of High-Pressure Overexpanded Planar Nozzle Flow Using a Simple, Low-Cost Test Apparatus," *Journal of Visualization*, Vol. 14, No. 1, 2011, pp. 11–14.

[23] Settles, G., *Schlieren and Shadowgraph Techniques*, Springer-Verlag, New York, 2001.

[24] Nasuti, F. and Onofri, M., "Shock Structure in Separated Nozzle Flows," *Shock Waves*, Vol. 19, 2009, pp. 229–237.

[25] Bayeh, A. and Karpetis, A., "Miniaturized Combustor for Methane-Air Afterburner," *Journal of Propulsion and Power*, Feb. 2012, Submitted.

[26] Texas A&M University, Aerospace Engineering, "Transient Flames," August 2010, [http://www.youtube.com/watch?v=chxdYtRqTOM. Accessed 08/25/10.]

[27] Glassman, I., *Combustion*, 4th ed., Academic Press, 2008, pp. 240–250.

[28] Van den Schoor, F., Hermanns, R., van Oijen, J., Verplaetsen, F., and de Goey, L., "Comparison and Evaluation of Methods for the Determination of Flammability Limits, Applied to Methane/Hydrogen/Air Mixtures," *Journal of Hazardous Materials*, Vol. 150, 2008, pp. 573–581.

[29] Favaloro, M., "Ablative Materials," *Kirk-Othmer Encyclopedia of Chemical Technology*, 2000.

[30] Mishra, C. and Yoav, P., "Incompressible and Compressible Flows Through Rectangular Microorifices Entrenched in Silicon Microchannels," *Journal of Microelectromechanical Systems*, Vol. 14, No. 5, Oct. 2005, pp. 1000–1012.

[31] Kee, R., *Chemically Reacting Flow: Thoery and Practice*, 1st ed., John Wiley & Sons, 2003, pp. 649–683.

[32] Goodwin, D., "An Open-Source, Extensible Software Suite for CVD Process Simulation," *Proceedings of CVD XVI*, 2003, pp. 155–162, [http://code.google.com/p/cantera/. Accessed 01/15/11.].

[33] Smith, G., Golden, D., Frenklach, M., Moriarty, N., Eiteneer, B., Goldenberg, C., Bowman, T., Hanson, R., Song, S., Gardiner, W., Lissianski, V., and Qin, Z., "GRI-Mech Source," [http://www.me.berkeley.edu/gri_mech/. Accessed 01/15/11.]

[34] van Rossum, G., "Python Programming Language - Official Website," [http://www.python.org/. Accessed 01/15/11.]

[35] Bergthorson, J. and Dimotakis, P., "Premixed Laminar C1-C2 Stagnation Flames: Experiments and Simulations with Detailed Thermochemistry Models," *Proceedings of the Combustion Institute*, Vol. 31, 2007, pp. 1139–1147.

[36] Odedra, A. and Malalasekera, W., "Eularian Particle Flamelet Modeling of a Bluff-Body CH4/H2 Flame," *Combustion and Flame*, Vol. 151, Aug. 2007, pp. 512–531.

[37] Hamamatsu Photonics, Iwata City, Japan, *Image Intensifiers*, Sept. 2009.

[38] Eckbreth, A., *Laser Diagnostics for Combustion Temperature and Species*, 2nd ed., Gordon and Breach Publishers, 1996.

[39] Navon, D., *Semiconductor Microdevices and Materials*, CBS College Publishing, 1986, pp. 387–397.

[40] Longmire, M., "SBIG Software - CCDOPS," [http://www.sbig.com/Software.html. Accessed 10/15/11.]

[41] Santa Barbara Instruments Group, Santa Barbara, California, *CCD Camera Operating Manual for the Model ST-4x, ST-5, and ST-6*, Jan. 1996, Revision 2A.

[42] Markerink, W., "Camera Mounts & Registers," [http://www.markerink.org/WJM/HTML/mounts.htm. Accessed 11/15/11.]

[43] Hiller, B., Paul, P., and Hanson, R., "Image-Intensified Photodiaode Array as a Fluorescence Detector in CW-Laser Experiments," *Review of Scientific Instruments*, Vol. 61, No. 7, July 1990, pp. 1808–1815.

[44] Welford, W., *Useful Optics*, 1st ed., The University of Chicago Press, 1991.

[45] Zare-Behtash, H., Kontis, K., Gongora-Orozco, N., and Takayama, K., "Compressible Vortex Loops: Effect of Nozzle Geometry," *International Journal of Heat and Fluid Flow*, Vol. 30, 2009, pp. 561–576.

[46] White, F., *Viscous Fluid Flow*, 3rd ed., McGraw-Hill, 2006.

[47] Platzer, M., Simmons, J., and Bremhorst, K., "Entrainment Characteristics of Unsteady Subsonic Jets," *AIAA Journal*, Vol. 16, No. 3, 1977, pp. 282–284.

[48] Bremhorst, K. and Harch, W., "The Mechanism of Jet Entrainment," *AIAA Journal*, Vol. 16, No. 10, 1978, pp. 1104–1106.

[49] Vermeulen, P., Ramesh, V., and Yu, W., "Measurements of Entrainment by Acoustically Pulsed Axisymmetric Air Jets," *ASME Journal*, Vol. 108, July 1986, pp. 479–484.

[50] Papamoschou, D. and Roshko, A., "The Compressible Turbulent Shear Layer: An Experimental Study," *Journal of Fluid Mechanics*, Vol. 197, 1988, pp. 453–477.

[51] Samimy, M., Reeder, M., and Elliott, G., "Compressibility Effects on Large Structures in Free Shear Flows," *Physics of Fluids*, Vol. 4, No. 6, 1992, pp. 1251–1258.

[52] Elliot, G. and Samimy, M., "Compressibility Effects in Free Shear Layers," *Physics of Fluids*, Vol. 2, No. 7, July 1990, pp. 1231–1240.

[53] Ricou, F. and Spalding, D., "Measurements of Entrainment by Axisymmetrical Turbulent Jets," *Journal of Fluid Mechanics*, Vol. 11, 1961, pp. 21–32.

[54] Tacina, K. and Dahm, W., "Effects of Heat Release on Turbulent Shear Flows. Part 1. A General Equivalence Principle for Non-Buoyant Flows and its Application to Turbulent Jet Flames," *Journal of Fluid Mechanics*, Vol. 415, 2000, pp. 23–44.

[55] Huh, H. and Driscoll, J., "Shock-Wave-Enhancement of the Mixing and the Stability Limits of Supersonic Hydrogen-Air Jet Flames," *Twenty-Sixth Symposium (International) on Combustion*, 1996, pp. 2933–2939.

[56] Driscoll, J., Huh, H., Yoon, Y., and Donbar, J., "Measured Lengths of Supersonic Hydrogen-Air Jet Flames – Compared to Subsonic Flame Lengths – and Analysis," *Combustion and Flame*, Vol. 107, 1996, pp. 176–186.

[57] Miller, M., Bowman, C., and Mungal, M., "An Experimental Investigation of the Effects of Compressibility on a Turbulent Reacting Mixing Layer," *Journal of Fluid Mechanics*, Vol. 356, 1998, pp. 25–64.

VITA

Name:	John L. Richards
E-mail Address:	jlrichards@tamu.edu
Address:	John Luke Richards c/o Department of Aerospace Engineering 701 H.R. Bright Building, Ross St., TAMU 3141 Texas A&M University College Station, TX 77843
Education:	B.S., Mechanical Engineering, Colorado School of Mines, 2010 M.S., Aerospace Engineering, Texas A&M University, 2012